Theses and Dissertations

2011

Finite Element Modeling of High Current Density Effects & Power Handling Capability of RF MEMS Capacitive Switches

Bora Baloglu
Lehigh University

Follow this and additional works at: http://preserve.lehigh.edu/etd

Recommended Citation

Baloglu, Bora

Electro-Mechanical Modeling and Simulation of RF MEMS Switches

January 2008

Electro-Mechanical Modeling and Simulation of RF MEMS Switches

by

Bora Baloglu

_____

A Thesis

Presented to the Graduate Research Committee

of

Lehigh University

In Candidacy for the Degree of

Master of Science

In

Mechanical Engineering

_____

Lehigh University
Bethlehem, Pennsylvania

January 2008

This Thesis is accepted and approved in partial fulfillment

of the requirements for the Master of Science

Herman F. Nied, Ph. D.
Thesis Advisor

Herman F. Nied, Ph. D.
Chair of Mechanical Engineering
and Mechanics Department

December 6, 2007
Date

ii

Acknowledgements

I would like to express my sincere appreciation to my advisor Professor Herman F. Nied for his continuous support, encouragement, and guidance throughout this research. His efforts towards my academic progress have been invaluable.

I also would like to thank Professor James C. Hwang, Professor Richard P. Vinci and Dr. Cristiano Palego for their contributions to this study.

I am very thankful to my family for their continuous encouragement and believing in me despite the miles between us. I especially would like to thank my mother, Nevin, who encouraged me to continue graduate study in the US.

A special thanks also to my friend Vera Partem for her encouragement and support when I was very far away from home.

Another special thanks to my undergraduate instructor Asst. Professor Bora Yildirim for guiding and inspiring me to come to Lehigh University.

I am also thankful to Mrs. Carol Paul, Mrs. Geri Kneller, and Mrs. Jennifer Smith for their kindness and administrative assistance. In addition, I thank all my friends in the Solid Mechanics Laboratory for their valuable contributions and friendship.

LIST OF FIGURES

LIST OF TABLES

ABSTRACT

Reliability is at the center of engineering studies in today's society. Electronic devices keep getting exponentially smaller by day and are now being used in almost everything that is vital in daily life, from the washing machine in the house, to the cell phone in one's pocket. As a result, the drive to better understand the development of these tiny structures has become increasingly significant through the study of Microelectromechanical Systems, also known as MEMS. MEMS are integrated mechanical elements such as actuators, sensors and electronics on silicon substrates. It is an interdisciplinary topic which is innovative to the field of Mechanical Engineering and requires in-depth understanding of electronics. Therefore, fabrication techniques and some of the basic electronics associated with MEMS are introduced in the first section of this study. The main focus in this study is RF MEMS Capacitive switches, which actuate mechanically by electrostatic forces as a result of an applied voltage. The commercial finite element code ANSYS is used for simulations and modeling. 3D models are utilized in the performed analyses. In the first part of the calculations, the spring constants of the membranes are calculated. The spring constant plays a significant role in determining the pull-in voltage for MEMS switches. Analytically calculated spring constant values are compared with the simulation results. Then, natural frequencies of the various switches are determined. By introducing viscoelastic material properties into the finite element models, the time dependent behavior of the membrane is studied. Transient analysis is performed for different hold and release times. Finally, the entire switch behavior is simulated under electrostatic forces using a coupled electrostatic analysis. In order to create the electrostatic forces, an air mesh is modeled by enclosing

the entire electromechanical system. The results include data on displacement versus voltage, capacitance versus voltage and the pull-in voltage. The results obtained in this study represent the minimum forces required for switch actuation, since residual stresses were not considered. It is believed that the addition of tensile residual stress will significantly increase the voltage (electrostatic force) needed to activate the MEMS Switches examined in this study.

1 Introduction

1.1 Microelectromechanical Systems

Microelectromechanical Systems (MEMS), also referred to as micro machines, are microscopic structures integrated onto silicon, which combine mechanical, optical and fluidic elements with electronics. The characteristic size of MEMS varies from a couple of microns to a centimeter. These systems can sense, control activate mechanical processes on the micro scale and function individually or in arrays to generate effects on the macro scale. The micro fabrication technology enables fabrication of large arrays of devices, which individually perform simple tasks, but in combination, can accomplish complicated functions. The development of microelectromechanical systems requires appropriate manufacturing technologies that enable features, such as the definition of small geometries, precise dimensional control, interfacing with control electronics, reliability, repeatability, design flexibility, high yield and low cost per device, systems of the twenty-first Century to emerge.

Smaller dimensions offer many operational advantages, such as soft springs, high resonance frequency and low thermal mass. However, it should be noted that it is not always beneficial to work at micron length scales. Some physical phenomena might perform poorly when the dimensions are reduced, whereas, another system works better when miniaturized. One can generally observe that smaller things are less affected by gravity, which allows faster speed and efficiency [1].

The main purpose of MEMS technologies is to integrate micro-mechanical systems with micro-electrical systems and to develop the combined structure.

3

Examples of MEMS device applications include inkjet-printer cartridges, accelerometers, miniature robots, microengines, locks, inertial sensors, micro transmissions, micro mirrors, micro actuators, optical scanners, fluid pumps, transducers and chemical, pressure and flow sensors.

1.1.1 Historical Background

In 1947, the first transistor was invented at Bell Telephone Laboratories. It resulted in a fast-growing microelectronic technology. In 1958, Jack Kilby of Texas Instruments built an integrated circuit (IC) using germanium device, which consisted of one transistor, three resistors and one capacitor. The IC was implemented on a sliver of Ge that was glued on a glass slide. In the same year, Robert Noyce of Fairchild Semiconductor announced the development of a planar double-diffused Si IC. In the following ten years, a complete transition from the original Ge transistors to silicon (Si) devices took place. Because of a decrease in the dimensions of the devices, the complexity of ICs has doubled every two to three years, starting in the 1970's. Today, the fabrication of more than 10 million transistors and capacitors on a classic chip is enabled with the technology of ultra-large-scale-integration (ULSI). IC fabrication is dependent upon sensors to provide input from the surrounding environment. As a result, the attention was first focused on microsensor development. The first microsensor, which has also been the most successful, was the Si pressure sensor [2].

The actual initiator of the Microelectromechanical Systems is known as physicist Richard P. Feynman. In 1959, he proposed the idea of producing distinctly small mechanical devices by evaporating or accumulating the materials [3]. In his important speech on this topic, he provided biological systems as examples. He explained that it is

4

possible to form tiny machines by, first, chemically synthesizing the materials, then, combining them physically at the atomic level. This idea was partly accomplished in the mid 1960's. During these years, the first examples of micro machines were being produced. Later, in the 1970's, important progress was accomplished on manufacturing techniques for combined micro devices. With new etching techniques, numerous micron level parts were fabricated by selectively removing areas of the Si substrate, in order to obtain the desired geometries. Towards the end of the 1980's, new surface micromachining techniques allowed integrated fabrication of mechanisms and introduced the serial fabrication of micromechanical parts, such as pressure-sensor diaphragms. The importance of surface micromachining is in the capability of forming micro-mechanical systems directly on an Si plate, which eliminates the cost of installation of micromechanical parts one by one [4]. In the 1990's, new lithography techniques made it possible to produce micro-mechanical systems and devices with very high aspect ratios. It should be noted that equivalent terms for MEMS, are 'microsystems' (Europe) and 'micromachines' (Japan).

1.1.2 Components of MEMS

MEMS are characteristically not bigger than a grain of sand. These devices are complex machines that enable chips to function mechanically. They act as the most direct links between digital electronics and the physical world. MEMS have four basic components. These are microelectronics, microsensors, microactuators and microstructures [5, 6].

Microelectronics act like the brain and control all of the data. Electronics receive the data and process it, after which, decisions are made accordingly. Electronics receive the data from the various microsensors.

Microsensors act as the arms, legs and eyes of MEMS. They detect information from the surrounding environment and pass this information on to microelectronics for processing. These sensors can monitor mechanical, thermal, biological, chemical, optical and magnetic readings from the surrounding environment.

A microactuator acts as a switch or a trigger to activate an external device. First, the microsensors receive data and process it. Then, the microactuator passes the data on to the microelectronics for decision making. Based on this decision, the microactuator moves and either actives or deactivates a device.

Microstructures act like valves to control the flow of a substance or very small filters. With the improvements in micromachining technology, it is possible to build extremely small structures, known as microstructures, onto the surface of a chip. These are built right into the Si of the MEMS.

1.1.3 Commercial Applications of MEMS

The potential of MEMS technology promises to reform our present-day life-styles as much as the computer has. Besides the completely new applications offered by MEMS technology, existing applications will most likely be replaced by miniaturized, low-cost and high-performance, MEMS technology. The most important thing MEMS offers is cost-effective and high-performance systems. Thus, it is attracting considerable attention from the government and a multitude of companies. However, the significant up-front investment required for successful, large-volume commercialization of MEMS, is likely

to limit the initial involvement to larger companies in the IC industry. These companies can force their existing capital investment in semiconductor processing equipment towards the development of MEMS components for large-volume applications [2].

MEMS are most popular in the automotive industry as accelerometers for airbag systems. They have many other uses besides airbag systems, and not only for the automotive market. Table 1.1 shows the commercial applications of MEMS for different markets.

Automotive Market	Consumer Market	Industrial Market
Airbag Systems	Appliances	Earthquake Detection and Gas Shutoff
Security Systems	Sports Training Devices	
Brake Lights	Computer Peripherals	Shock and Tilt Sensing
Headlight Leveling	Navigation Devices	
Rollover Detection	Active Subwoofers	Machine Wellbeing
Automatic Door Locks	Active Suspension	

Table 1.1: Commercial Applications of MEMS [2].

1.2 Objective of Research

The main goal of this research project is to develop the models to simulate RF MEMS Capacitive switches. However, in the beginning of the thesis, the basic manufacturing techniques are introduced in order to obtain a better understanding of MEMS structures. Later, the mechanics of the membrane behavior are studied via simple membrane shape examples. Since membrane movement is a direct result of electrostatic forces, it is also important to understand the electrostatics of RF MEMS switches. Therefore, the electrostatics section reviews the required electrical formulas. The coupling between the mechanical and the electrical fields serves as a significant

7

justification for a better understanding of the inner-workings of the RF MEMS Switch. The modeling section describes the meshing details and the 3D models that have been used in the simulations. Different membrane designs are examined in this study and proper meshing is performed in great detail in order to obtain a more in-depth comprehension of the subject. These different membrane designs are taken from switches that have been tested in the Compound Semiconductor Technology Laboratory at Lehigh University. Natural frequencies and modal shapes of the membranes are obtained with a modal analysis. The spring constant, which plays a significant role in the calculation of the pull-in voltage, is also extracted. Since the main idea of this elastic analysis is to obtain the spring constant, instead of simulating the electrostatic actuation, the membrane has been displaced by applying a surface force. Using this spring constant and the analytical formulas, the pull in voltage is also calculated for later comparisons. Additionally, a viscoelastic analysis is completed with time dependent material properties in order to observe the viscoelastic behavior of the membrane. Here again, the desired material behavior is obtained by specifying displacements rather than electrostatic forces. And finally, the electromechanically coupled problem is solved for the switch system. The results include the voltage displacement behavior, a calculation of the pull-in voltage and the capacitance-voltage relationships. In the conclusion, the results are discussed and comparisons are made between different membrane designs.

2 Microtechnology

MEMS technology is based on a number of tools and methodologies, which are used to form small structures with dimensions at the micron level. A significant part of the technology has been adopted from integrated circuit (IC) technology. As an example, almost all devices are built on wafers of silicon. The structures are realized in thin films of materials, just as for the ICs. Similarly as with the ICs, they are then patterned using photolithographic methods. However, as the MEMS technology advances, several innovative fabrication techniques will become customary to use for the fabrication of microelectromechanical systems.

Microtechnology has three basic steps: (1) depositing different kinds of materials on a substrate, (2) applying a patterned mask on top of the films for each layer, and (3) removing the needless parts. Detailed fabrications processes will be explained next. This section is based heavily on material from references [5, 7, 8].

2.1 Deposition

There are generally two types of deposition techniques used in microelectronics and micromaching. These are Chemical Vapor Deposition (CDV) and Physical Vapor Deposition (PVD). CVD involves diffusion with chemical reactions as well as convective heat and mass transfer at the substrate surface. On the other hand, in the PVD technique, the particles hit the hot substrate surface directly. In essence, CVD is a much more complex process when compared with the PVD techniques. However, the advantage of the CVD method is that it provides better overall quality of the deposition and the rate of growth.

2.1.1 Chemical Deposition

2.1.1.1 Chemical Vapor Deposition (CVD)

The schematic view of the CVD can be seen in Figure 2.1. In this figure, the substrates are placed in a reactor, with heaters on both the bottom and the top. In this process, the gas with the diffused reactants flows over the hot surface of the substrate. While the gas flows over the surface, the chemical reaction occurs as a result of the energy supplied from the temperature of the hot surface. Then, the by-products and the gas are vented. As a result of this chemical reaction, the reactants form a thin film on top of the substrate surface. The formation of the film happens during and after the reaction.
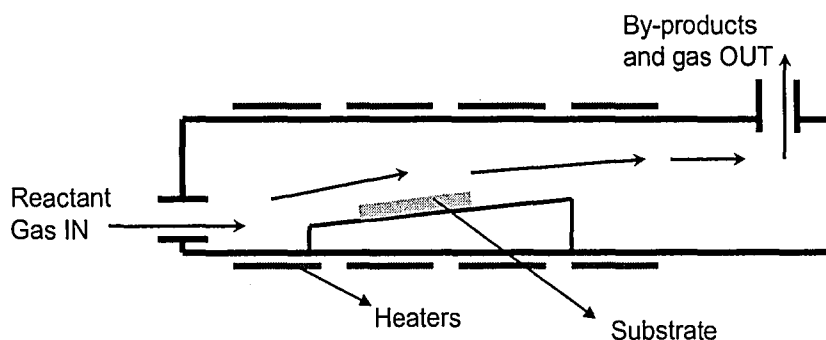
Figure 2.1: Schematic view of a Horizontal CDV System.

There are two important CVD technologies in MEMS. The first one is the Low Pressure CVD (LPCVD), which produces layers with excellent uniformity of thickness and material properties. However, this process requires high deposition temperatures (> 600°C) and the deposition rate is quite slow. The second technology is the Plasma Enhanced CVD (PECVD). Since the plasma provides energy to the gas molecules in this process, it can activate at lower temperatures (~300°C). On the other hand, the quality of the product is not as good as that of the LPCVD. Also, the PECVD can only deposit the material on one side of the wafer, whereas the LPCVD can affect both sides.

10

2.1.1.2 Electrodeposition

This process can be applied only to conductive materials. The typical set up can be seen in Figure 2.2. There are two plating techniques, known as electroplating and electroless plating. The first technique consists of another electrode (usually platinum) and an external electrical potential. In the electroplating process, can be seen from Figure 2.2, the substrate is placed in the electrolyte solution along with the second electrode. When an electrical potential is applied to the electrodes, a chemical reaction occurs. As a result of this reaction, a metal layer forms on the substrate. Additionally, the reaction causes some gas formation on the counter electrode.

The second technique is known as electroless plating, which does not need any external electrical potential. In this process, the chemical reaction occurs with the help of a more complex electrolyte solution. The deposition happens spontaneously and is very hard to control. As a result, it is preferable to use electroless plating since it does not require an external potential energy. One downside of this method is that it is very difficult to control the thickness and uniformity with this deposition technique.
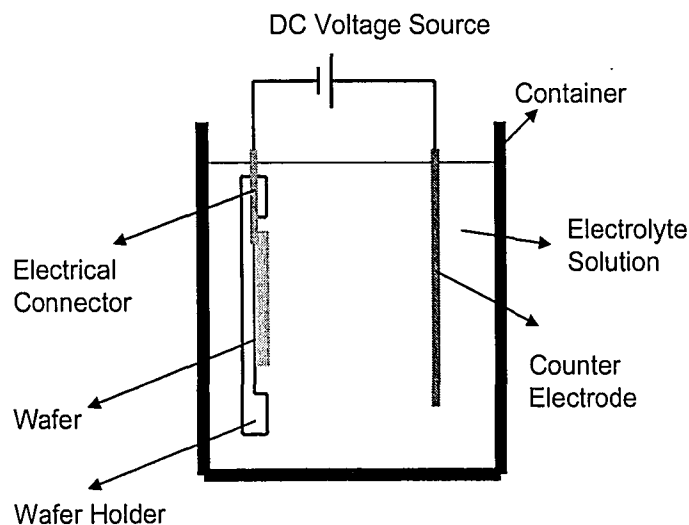
Figure 2.2: Schematic view of the set up for electrodeposition.

11

2.1.1.3 Thermal Oxidation

This is one of the most basic technologies and is limited to materials that can be oxidized. The schematic view of the process can be seen in Figure 2.3. The process starts with placing the wafers into the furnace, where the temperature is kept between 800°C-1100°C. The thermal oxidation process can be differentiated into two different ways - dry and wet oxidation. In the dry oxidation method, the oxygen gas is directly sent into the furnace, which in turn reacts with the Si on the wafer surface. In the wet oxidation process, water vapor is sent into the furnace. Despite the fact that it takes a longer time to form a layer via the dry oxidation method, the resulting quality is much better. In comparison, the wet oxidation process is much faster and better for thicker oxides. This method is used to process silicon dioxides and silicon substrates.
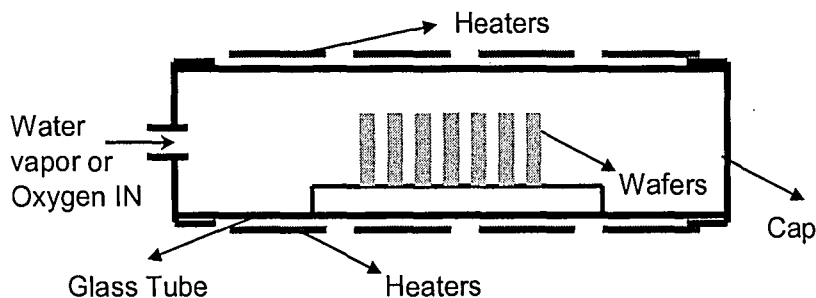
Figure 2.3: Schematic view of Thermal Oxidation

2.1.2 Physical Deposition

2.1.2.1 Physical Vapor Deposition (PVD)

This process releases the material from a source and transfers it to the substrate. There are two important physical vapor deposition techniques, which are evaporation and sputtering. Thermal evaporation is one of the oldest thin film deposition techniques. It is based on the boiling off of a heated material onto a substrate in a vacuum. On the

contrary, sputtering is the removal of the material from the source at a much lower temperature than evaporation.

2.1.2.2 Thermal Evaporation

The typical set up for thermal evaporation can be seen in Figure 2.4. In this process, the material in the source bottle is heated up by the applied current. This heat causes the source material to boil and to evaporate. The vacuum is required for the molecules to freely evaporate in the chamber. Subsequently, these free molecules condense on all of the surfaces. The overall principle is the same for all types of evaporation techniques; however, different techniques are being used to heat the source material. The two main types of techniques utilized for heating source materials are e-beam evaporation and resistive evaporation.
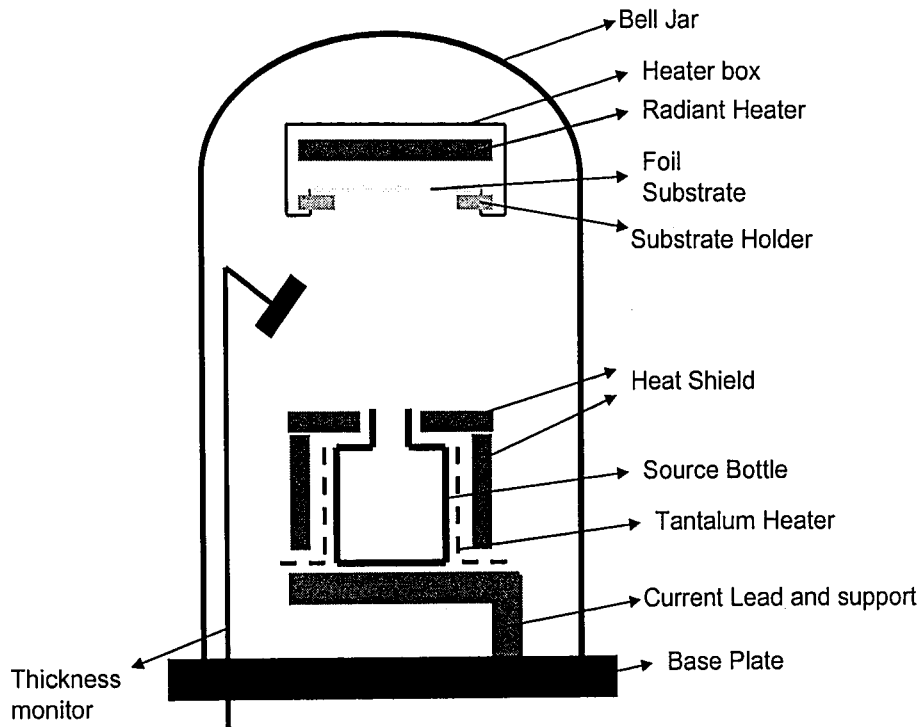
Figure 2.4: Schematic view of a typical evaporation set up.

13

2.1.2.3 Sputtering

Sputtering is very similar to the evaporation techniques, but happens at much lower temperatures than evaporation. In this process, the substrate and the material sample are placed in a chamber similar to that used for evaporation. An inert gas is introduced into the chamber at a low pressure. A gas plasma is struck using an RF power source, resulting in the gas becoming ionized. The target, a disc of the material to be deposited at a high negative potential, is bombarded with positive inert gas ions created in the plasma. As a result of this bombardment, the deposition material evaporates and condenses on the surface of the substrate and everywhere in the chamber. Considering all of the specifics regarding each evaporation technique, sputtering is actually preferred in most applications as opposed to evaporation due to its work capability with a wider range of materials.

2.2 Lithography

Lithography is the process of transferring a pattern to a photosensitive material using a radiation source, such as light. The photosensitive material experiences a change in its physical properties when exposed to a radiation source. In order for this to happen, first, all of the wafer surface needs to be cleaned in appropriate solutions from atmospheric dust, abrasive particles, dust from scribing, and other such materials. After the cleaning process, the wafer is held on a spinner as it shown in Figure 2.5. The resist is coated to uniform thickness by spin coating. It typically spins for 15-30 seconds, with speeds ranging between 3000-6000 rpm.

14
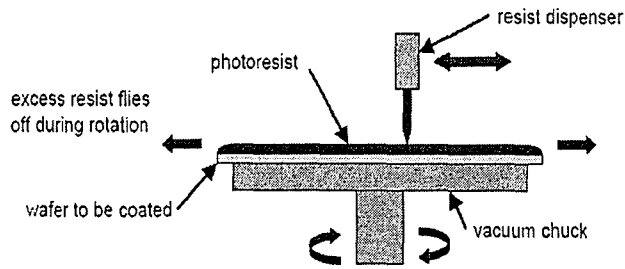
Figure 2.5: Photoresist Spin Coating illustration.

The next step is to bake the wafer in order to have a denser resist on the wafer. Then, the wafer goes under a specifically designed mask containing the desired pattern, allowing the alignment to take place. Following the alignment phase, the wafer is exposed to radiation. (The mask prevents the covered parts from being exposed to the radiation source and only exposes the uncovered part). Thus, the pattern that is desired will be imprinted on the photosensitive material. The imprinted mask separates the areas into two: the exposed and the unexposed.

In Figure 2.6, the next step of the process is shown, in which the imprinted pattern is developed in a wet solution. Depending on the photoresist, this can be done either by a process known as positive lithography, in which the exposed parts are removed, or by negative lithography, a process in which the unexposed parts are removed.
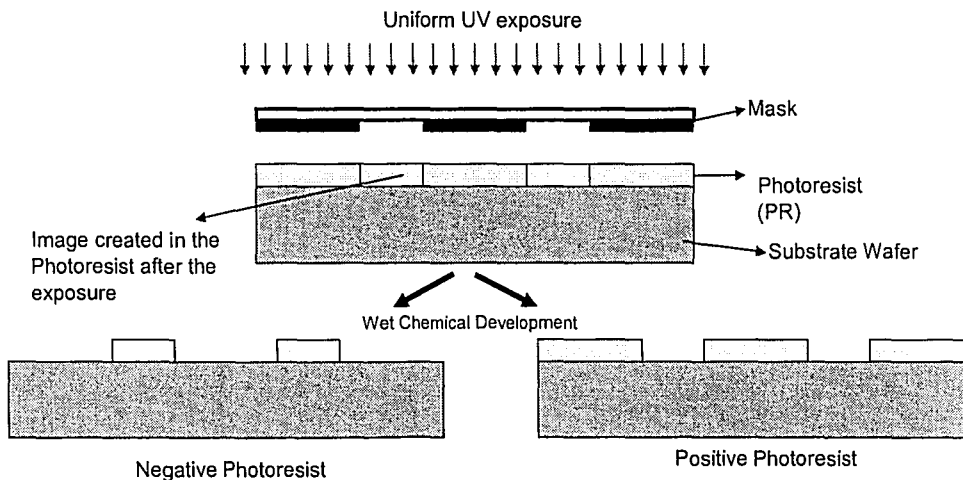
Figure 2.6: Schematic view of the positive and negative photoresists.

As a final step, after the development of the desired pattern, the wafer goes through the baking process once more, known as the hard bake. This step hardens the photoresist on the wafer and makes it ready for later processings. If more than one layer needs to be patterned, the same process should be followed.

2.3 Etching

This process involves the removal of underlying material, which is no longer protected by the photoresist after development. The etching process can be isotropic or anisotropic. If the etching takes place at the same rate in all directions, it is called isotropic. Conversely, if the rate differs for different directions, it is called anisotropic. There are two main types of the etching processes: wet etching and dry etching.

2.3.1 Wet Etching

Wet etching is a very simple process – it can be done with a container full of solution that will dissolve all of the material that needs to be removed. The chemical solution used in wet etching attacks the parts of the substrate that are not protected by the mask. Wet etching involves inexpensive equipment and facilities for processing. It is also a faster etching process than the dry etching. However, it often results in poor quality of etched surfaces due to bubbles and flow patterns of the solution.

2.3.2 Dry Etching

This technology is more expensive than the wet etching technology. However, it gives a very fine resolution on the substrate surface. Dry etching involves the removal of the substrate materials by gaseous enchants without wet chemicals or rinsing. There are

three types of etching techniques: (1) Plasma Etching, (2) ion milling, and (3) reactive ion etching.

Plasma etching involves the addition of chemically reactive gasses into the plasma, a neutral ionized gas carrying a large number of electrons and positively charged ions, generated along with the RF energy source. The etching of these materials is accomplished by the high-energy ions found in the plasma bombarding the substrate surface with simultaneous chemical reactions between the reactive neutral ions and the substrate. This high-energy reaction causes local evaporation, resulting in the removal of the substrate material. The illustration can be seen below, in Figure 2.7.
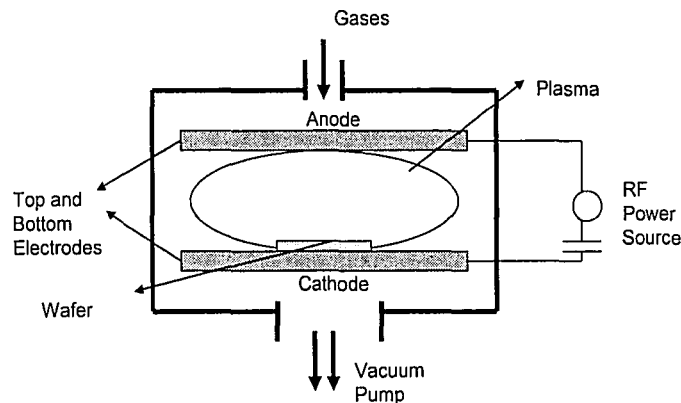
Figure 2.7: Schematic view of the RF Plasma Etching.

Ion milling, also known as ion-beam etching, is a process in which a beam of ions strike a sample, transfer their momentum to the sample surface, and thus, remove one or more atoms from the surface. Typically, an ion source injects ions into a vacuum chamber. The beam is lined up, accelerated, and finally, it strikes the sample, thereby removing atoms from its surface.

Another one of the dry etching techniques is called Reactive Ion Etching. It is a process via which the chemical etching is accompanied by ionic bombardment. The bombarded ions open up a space for chemical reactions, making it more efficient.

In the previous sections, MEMS, their fabrication techniques and commercial applications were explained in order to provide the background material about these devices. The next section contains the main focus of this study and examines the electromechanical behavior of MEMS for Radio-Frequency circuits (RF MEMS). In particular, RF MEMS Switches will be introduced.

3 RF MEMS

In MEMS technology, radio frequency (RF) is defined as the rate of oscillation within the range of 3Hz and 300GHz [5]. This range corresponds to the frequency of an alternating current (AC), via which electrical signals are used to produce and to detect radio waves. MEMS refers to the specific sub-millimeter sized parts which need to move for the components to have electronic functionality. In order to achieve high cut-off frequencies of switching devices for low-loss applications, MEMS technology needed some enhancements. Such examples of RF MEMS come in the form of capacitors, inductors, resonators and switches. The cut-off frequency is the frequency that is a boundary in the system response at which point the energy entering the system begins to be reflected instead of transmitted [5]. During the past twenty years, the progress in these technologies has not been adequate enough to meet the needs of the industry which was to increase the cut-off frequencies. For instance, the cut-off frequency of CMOS transistors was around 500MHz, and now it is around 100GHz. RF MEMS technology has accomplished up to 40,000 GHz cut-off frequencies and has been growing very fast in the past ten years. RF MEMS research can be grouped into four different areas [9].

These are; 1) RF MEMS switches, varactors (voltage controlled capacitors) and inductors, 2) RF Micromachined transmission lines, filters and antennas, 3) FBAR (thin film bulk acoustic resonators) and filters and 4) RF Micromechanical resonators and filters. Since the main interest of this research project is in the RF MEMS switches, they will be explained in great detail. Further details on the other areas of RF MEMS mentioned here can be found in references [10-12].

4 RF MEMS Switches

RF MEMS Switches exhibit closely coupled mechanical/electrical behavior. The mechanical movement of the switch is achieved by utilizing electrostatic, magnetostatic, piezoelectric or thermal designs. In current industry, the electrostatic and magnetostatic switches have high reliability and high frequencies [9]. Magnetostatic actuation requires low voltages and has high switching speeds and a relatively high current consumption. Thermal actuators require low voltages and have high switching speeds as well, but once again, they exhibit a high current consumption. Hence, electrostatic actuation is the preferred type for MEMS switches. It not only has a very low to no current consumption, but it also has high switching speeds.

RF MEMS switches can be categorized by the contact types: 1) capacitive switches (metal-insulator-metal) [13-15] , and 2) resistive switches (metal-metal) [16, 17]. Capacitive switches use a thin layer of dielectric that prevents the metal-metal contact. It also reduces the likelihood of stiction, where the membrane does not release after contact with the dielectric layer, mainly due to charge accumulation. However, the dielectric layer will only conduct signals with reasonable insertion loss (the loss of transmitted signal power between a source and a load) when coupling between the conductor electrodes is above a certain frequency [18].

RF MEMS Switches are widely used in Phased Array Radar systems. These are basically group of antennas in which the relative phases of the respective signals feeding the antennas are varied [5]. In these systems the variation of the signals are controlled by using RF MEMS Switches. Essentially, they modify the velocity of the signal propagated through the feeding transmission line. The activation in the switch changes the

capacitance. The change in the capacitance allows RF MEMS switch to control the velocity of the signal which permits managing the radiation pattern (directional dependence of radiation from the antenna) characteristics very precisely.

Electrostatic actuation is very simple to apply since it only requires two electrodes. The actual mechanical movement is due to the electrostatic forces between the electrodes. Typical electrostatic actuation occurs when the membrane, in the form of a movable electrode, is subjected to an electrostatic force during the application of a voltage between two conductors. Figure 4.1 shows the schematic view of the actuated switches in the ON and OFF positions. The electrostatic force causes the membrane to deform and, in turn, contact the lower electrode, placing the switch into the ON position. When the applied voltage is removed, the membrane "snaps" back into its original OFF position. The 'V_p' (pull-in voltage), is the voltage value that causes the membrane to actually move down and make contact with the lower electrode.

In essence, there are two different switch structures of this type. The first one is known as the fixed-fixed beam structure, while the second one is fixed at only one end of the cantilever beam structure. The fixed-fixed bridge structure RF MEMS switch is the focus of this research work, since a parallel experimental effort is being conducted to measure the pull-in voltages of the different types of membrane designs.
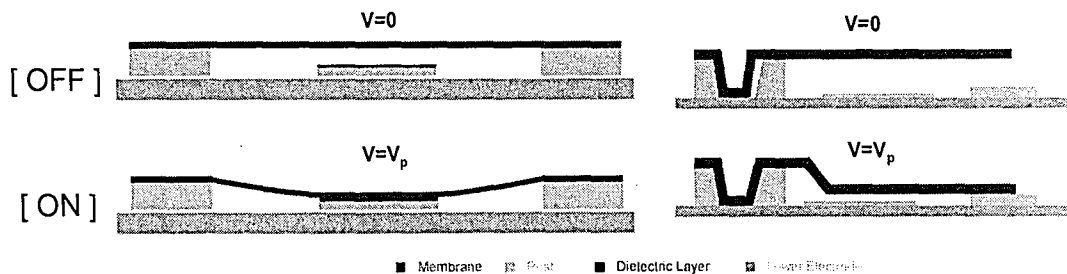
Figure 4.1: Schematic diagram of the (a) fixed-fixed beam and (b) Cantilever beam Switch

21

The pull-in voltage range for these types of switches changes between 10V and 100V. The required voltage for the actuation depends on the membrane thickness, material and the working environment. Another important thing to consider is the changing gap between the electrodes. The nonlinearity of the electrostatic force does not permit precise control of the switch at voltage levels below the pull-in voltage [19]. The nonlinearity will be explained in detail in the mechanics sections.

4.1 Mechanics of RF MEMS Switches

Understanding the mechanical behavior of MEMS is important in order to obtain information about how the membrane will behave under different types of loads and environmental conditions. In this case, the mechanical movement is due to electrostatic forces. Since beam structures are well studied in the literature, one can apply various forces, observe the behavior of the membrane and compare the experimental results with various simulation models.

The first thing to consider in regards to mechanical behavior of the switches should be the process of calculating the spring constant. Since most of the RF MEMS switch movements consider small deflection, the mechanical behavior can be modeled by using a linear spring constant. This section is a synopsis of the material given in reference [9]. The figures and equations are taken directly from this reference.

The spring constant, k (N/m), can be calculated by;

$$k = \frac{F}{\Delta g} \tag{4.1}$$

where, Δg (m) is the gap deflection, and F (N) is the external force. The fixed-fixed bridge structures are preferable because of their high spring constants and ease of

22

manufacturing. Spring constant determination is investigated by dividing the behavior into two parts. These are designated k_1 and k_2. The first part, k_1, which is due to its material characteristics (stiffness and moment of inertia) and the second part, k_2, because of the biaxial residual stresses created during the manufacturing process.

The k_1 determination is performed for different force applications. For example, the force is distributed over the whole membrane, over one third of the membrane or a single centered vertical force. Again, it is well known from the beam studies in the literature that the change in the external force location will affect the spring constant.

Below, different application of external forces examined for determination of the first part of the spring constant, k_1.
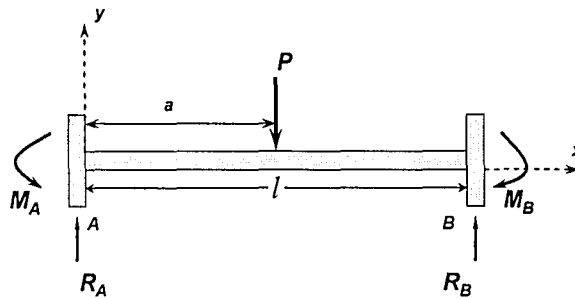
Figure 4.2: Concentrated vertical load on a fixed-fixed beam

Figure 4.2 shows that a fixed-fixed beam structure with a single force P centered on the membrane. Given in reference [20];

$$M_A = \frac{-Pa}{l^2}(l-a)^2$$

$$R_A = \frac{P}{l^3}(l-a)^2(l+2a)$$

(4.2)

23

$$EI\frac{d^2y}{dx^2} = M_A + R_A x \quad \text{for } x \le a$$

$$y = \frac{M_A x^2}{2EI} + \frac{R_A x^3}{6EI} \quad \text{for } x \le a$$

(4.3)

where, l is the length of the beam, E young's modulus and moment of inertia I is given by $I = wt^3/12$ for a rectangular cross section beam; w is the width of the beam and t is the thickness of the beam. M_A (N/m) is the reaction moment on the left end and, R_A is the vertical reaction on the left end. Therefore, the deformation in the center for this type of loading can be calculated by substituting $x = l/2$ into Equation (4.3). Then, Equation (4.1), the deflection and the force value will give the spring constant for this type of loading with $F = P$ and $\Delta g = y(l/2)$.
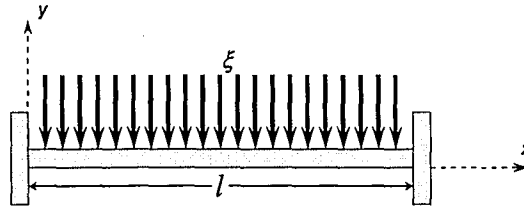
Figure 4.3: Distributed load on a fixed-fixed beam

As a second different application of force, Figure 4.3 shows a distributed load on the entire beam. Here, the deflection can be found by using superposition principle;

$$y = \frac{2}{EI} \int_0^l \frac{\xi}{48}(l^3 - 6l^2 a + 9la^2 - 4a^3)da$$

(4.4)

where, $P = \xi l$ and ξ is the load per unit area. Hence, the spring constant for this case would be [9];

$$k_1 = \frac{-\xi l}{y} \quad \text{or} \quad k_1 = 32Ew(\frac{t}{l})^3$$

(4.5)
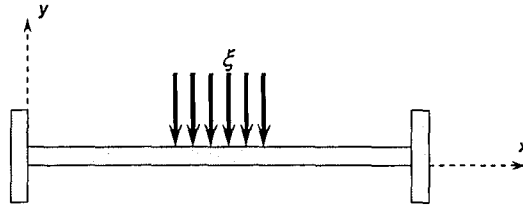
Figure 4.4: Distributed load about the center of the fixed-fixed beam

Figure 4.4 shows the force distributed on one-third of the beam in the center. For this case, the spring constant can be calculated by substituting $x = 2l/3$ into the below equation;

$$k_1 = 32Ew(\frac{t}{3})^3 \frac{1}{8(x/l)^3 - 20(x/l)^2 + 14(x/l) - 1}$$ (4.6)

In this section, the basic calculations for finding the spring constant for different load types are introduced. These will be used later to compare the simulation results with the analytical results. A rectangular membrane design is used to simulate different applications of forces on the membrane in the finite element calculations. The reason to do that is rectangular membrane dimensions are easy to apply to the analytical equations. Example design dimensions are 300 µm x1 µm x80 µm. The spring constant is found to be higher for the load distributed over the entire beam (Figure 4.3) than the spring constant calculated with distributed center focused load (Figure 4.4). This also varies depending on the material, since the formulation includes the E Young's modulus. In addition, it should be noted that an increase in the thickness of the membrane causes a drastic increase in the spring constant. For instance, a gold membrane with the dimensions of 300 µm x1 µm x100 µm has a spring constant of $k=9.5$ (N/m). On the other hand, the same material with a thickness of $t=2$µm has a spring constant of $k=76$ (N/m) [9].

25

As already mentioned earlier, the spring constant has an additional second part, resulting from the uniaxial residual stresses from the manufacturing process. This part should be calculated and added to the first part in order to have a realistic spring constant value to compare with the simulation results.

According to reference [21], uniaxial stress is calculated by modeling the membrane as seen in Figure 4.5. The membrane is analyzed when it is stretched by a concentrated vertical force that increases the stress in the membrane.
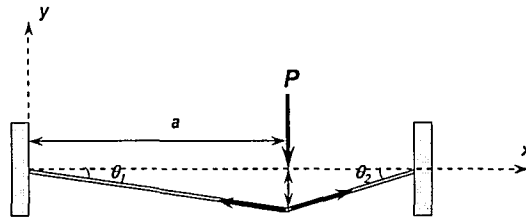
Figure 4.5: Stretched fixed-fixed beam with a concentrated vertical load

Here, note that the model only applies for tensile stress. Stress in the membrane increases the pulling forces on the ends in the amount;

$$\sigma + \frac{AE\Delta_1}{a} \qquad \text{where;} \quad \Delta_1 = \sqrt{a^2 + u^2} - a$$

$$\sigma + \frac{AE\Delta_2}{(l-a)} \qquad \qquad \Delta_2 = \sqrt{(l-a)^2 + u^2} - (l-a)$$

(4.7)

Since the deflection is very small, the increase in the force can be neglected and the deflection can be found by;

$$u = \frac{Pa(l-a)}{\sigma l}$$

(4.8)

Therefore, the stress part of k can be calculated by substituting $x = (l/2)$ for a force distributed over the entire beam and $x = (2l/3)$ for a force distributed over the one third of the membrane into the Equation 4.9.

$$k_2 = 8\sigma(1-\nu)w(\frac{t}{l})\frac{1}{3-2(x/l)} \qquad (4.9)$$

where, ν is poison's ratio and w is the width.

Hence, the spring constant is calculated by including the material stiffness and the uniaxial stresses from the manufacturing processes:

1. For the force distributed over the entire length of the beam:

$$k_t = 32Ew\left(\frac{t}{l}\right)^3 + 8\sigma(1-\nu)w\left(\frac{t}{l}\right) \qquad (4.10)$$

2. For the force distributed over the center of the beam (1/3$^{\text{rd}}$):

$$k_t = 32Ew\left(\frac{t}{l}\right)^3\left(\frac{27}{49}\right) + 8\sigma(1-\nu)w\left(\frac{t}{l}\right)\left(\frac{3}{5}\right) \qquad (4.11)$$

The above formulas are for static loading and will subsequently be used to compare some of the finite element simulation results. When electrostatic forces are taken into account spring constant determination should be considered in more complex forms, since actual electrostatic switching cannot be represented by simple force applications.

4.2 Electrostatics of RF MEMS Switches

As explained earlier, the voltage applied between two electrodes creates the electrostatic force resulting in pull down at the upper electrode (membrane). This is well known parallel plate capacitor behavior which introduces electrostatic forces due to the applied voltage. The parallel plate model helps to examine the basics of the electrostatics of the MEMS [22].

The capacitance between two plates can be calculated by knowing the area of the lower electrode, A, the permittivity of the air, ε_0 (8.85×10^{-12} F/m), and the gap, g ;

$$C = \frac{A\varepsilon_0}{g} \qquad (4.12)$$

According to reference [22], by considering the power delivered to a time dependent capacitor, the electrostatic force can be found as follows;

$$F_{elec} = \frac{1}{2}V^2 \frac{dC(g)}{dg} = -\frac{1}{2}\frac{A\varepsilon_0 V^2}{g^2} \qquad (4.13)$$

where, V is the applied voltage. However, this formula does not include the dielectric layer effect. By setting the mechanical restoring force from equation (4.1), equal to the applied electrostatic force from equation (4.13) and solving for voltage, results in;

$$V(g) = \sqrt{\frac{2k}{A\varepsilon_0}g^2(g_0 - g)} \qquad (4.14)$$

where, V is the voltage, k is the spring constant, A is the area of the lower electrode, ε_0 is the permittivity of the air and g_0 is the initial gap. The gap changes with the applied voltage and the membrane becomes unstable when it comes down to one-third of the total gap distance. In terms of the electric filed E, the electrostatic force is given by [22];

$$F_{elec} = \frac{QE}{2} \qquad (4.15)$$

where, $E = V/g$ is the electric field and Q is the charge. It can be easily shown that when the membrane is at the two-thirds of the gap height, the increase in the electrostatic force is greater than the increase in the restoring force (Equation 4.1), which makes the membrane position unstable and snaps it down. Substituting the unstable position height

($2g_0/3$) into Equation 4.16, one can calculate the pull-in voltage in terms of the initial configuration:

$$V_{pull-in} = \sqrt{\frac{8k_t}{27A\varepsilon_0}g_0^3} \qquad (4.16)$$

Since the spring constant depends on different force application models, the stiffness of the membrane and the residual stresses play a significant role, along with the spring constant, in determining the pull-in voltage. Also notice that these analytical formulas apply specifically to rectangular shapes. Therefore, all of the other membrane designs need to be analyzed using the finite elements method. In this research document, the first type of membrane design, also known as the simple rectangular shape design, will be used to compare these analytical results with the finite element simulation results.

The initial stress effect is not considered in the finite element simulation for determining the pull-in voltage. Therefore, Equation 4.16 is used to calculate the pull-in voltages analytically by substituting, $k_t = k_1 + k_2$, values from Equation 4.10 and 4.11. Appropriate material properties for gold are used.

Table 4.1 (a) and (b) shows the calculated pull-in voltage values from the strength of materials calculations for various initial stresses.

Applied force is over the entire membrane		
Initial Stress (Mpa)	Spring Constant including the initial stress effect (k_t)	Pull-in Voltage (V_p) (Volts)
10	19.53	20.03
20	31.48	25.43
30	43.43	29.87
40	55.37	33.73
50	67.32	37.19

(a)

Applied force is over the 1/3rd of the membrane in the center		
Initial Stress (Mpa)	Spring Constant including the initial stress effect (k_t)	Pull-in Voltage (V_p) (Volts)
10	11.35	15.27
20	18.52	19.51
30	25.68	22.97
40	32.85	25.98
50	40.02	28.67

(b)

Table 4.1: Pull-in Voltages for (a) force applied to the entire membrane surface and (b) with force applied to 1/3rd of the membrane surface

Residual stress in the membrane resulting from manufacturing can vary considerably and its effect on the pull-in voltage cannot be neglected. Therefore, it is very important to know the magnitude of the initial stresses on the membrane.

In general, the uniaxial residual stress varies between 20MPa and 50MPa. The example results given in Table 4.1 are for these initial stress values. Results are within the expected voltage range obtained in experimental measurements.
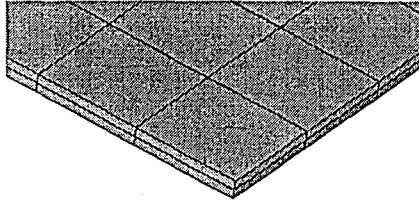
5 Spring Constant Calculation by Using FEM

In this section, the main purpose is to calculate the spring constant for different load applications using FEM models. The FEM simulations were performed to assess the accuracy of the strength of materials models given in section 4.2 and to prepare for calculation of the spring constants for more complex switch geometries.

In this section, rectangular membrane switch designs are considered. In particular, a 1μm thick gold membrane with dimensions of L (bridge length) = 300 μm and w (membrane width) = 80 μm is examined in detail. The micrograph of a rectangular membrane design (with slightly different dimensions) can be seen in Figure 5.1.
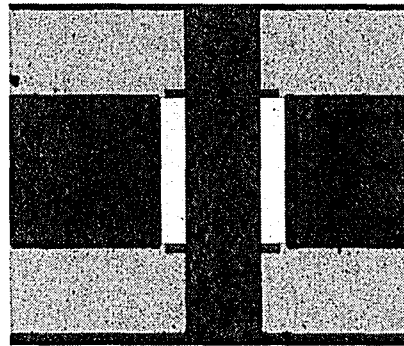
Figure 5.1: Micrograph of a rectangular membrane design.

Two different types of loadings are discussed here. First, the force distributed uniformly over the entire beam is considered. Figure 5.3 shows the finite element model with the force applied to the membrane and the boundary conditions (both ends of the membrane are fixed in the X and Y directions and the deformed profile of the membrane). In this model, SOLID95, twenty node structural hexahedron elements were used. The model has a total of 2500 elements, with two layers of elements through the thickness (Figure 5.2).

31

Figure 5.2: Elements through the thickness of a rectangular shaped membrane.

The formulas given in section 4.2 to determine the spring constant are for static loading; therefore, a static solution is also performed in ANSYS, i.e. inertia effects are assumed to be negligible. Maximum deflection is observed right in the middle of the membrane, as expected. The deflection value, Δg (m), from the FEM simulation is used in the spring constant formula, $k = \dfrac{\Delta g}{F}$ where k (N/m) is the spring constant and F (N) is the external force. According to this formula, Equation 4.1, the determined spring constant for the uniformly loaded (300 μm x 80 μm) membrane is $k = 5.87$ [N/m]. Later, this value will be used to determine the analytical pull-in voltage.

Figure 5.3: Applied force, boundary conditions and the deformed profile.
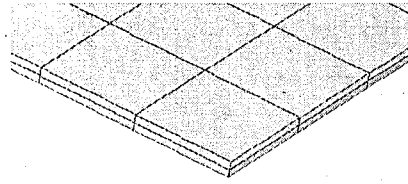
Figure 5.2: Elements through the thickness of a rectangular shaped membrane.

The formulas given in section 4.2 to determine the spring constant are for static loading; therefore, a static solution is also performed in ANSYS, i.e. inertia effects are assumed to be negligible. Maximum deflection is observed right in the middle of the membrane, as expected. The deflection value, Δg (m), from the FEM simulation is used in the spring constant formula, $k = \dfrac{\Delta g}{F}$ where k (N/m) is the spring constant and F (N) is the external force. According to this formula, Equation 4.1, the determined spring constant for the uniformly loaded (300 μm x 80 μm) membrane is $k = 5.87$ [N/m]. Later, this value will be used to determine the analytical pull-in voltage.

ΛN

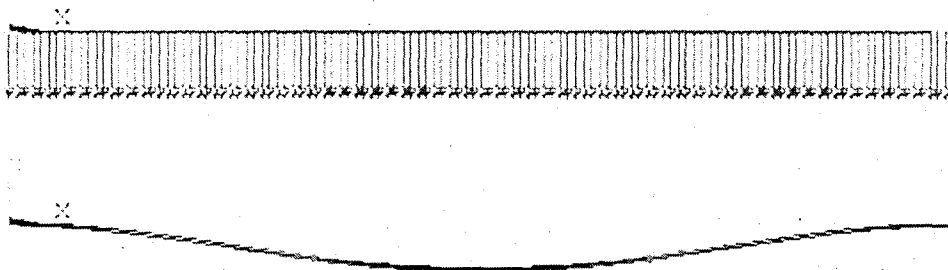**Figure 5.3:** Applied force, boundary conditions and the deformed profile.

The second load example is for the distributed force applied symmetrically to one-third of the membrane. This is done by specifying a loading area in the middle of the membrane. The static analysis is repeated for this type of loading and the deflection is determined. Figure 5.2 shows the loading and the deformed profile of the membrane. The same relationship between the force and the deflection (Equation 4.1) is used to determine the spring constant for this loading type.
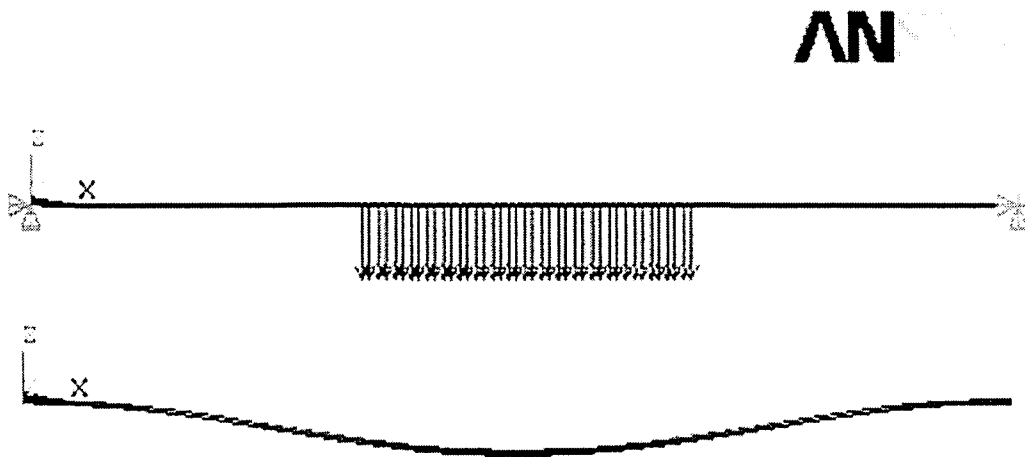
Figure 5.4: Applied force, boundary conditions and the deformed profile for 1/3rd loading.

The spring constant for this type of loading, geometry and material is found to be $k = 3.94$ [N/m]. This value is also used in the calculation of the analytical pull-in voltage.

Knowing the material properties of gold and using the analytical equation for the spring constant, which are explained in the mechanics of MEMS section (Section 4), the analytical value of the spring constant is determined for the two different load application methods. Table 5.1 shows the numerical values of the spring constants for both the simulation and the analytical strength of materials calculations:

Analysis Type	Spring Constant (k) N/m	
	Over the entire membrane (Case 1)	1/3rd of the membrane in the center (Case 2)
Analytical	7.58	4.14
ANSYS	5.87	3.94

Table 5.1: Numerical values of spring constants.

As can be seen from Table 5.1, the k spring constant simulated in case 1 differs from the k calculated analytically. This is primarily due to the fact that 3D elements were utilized in the simulation. The 3-D elements permit a more complex stress state near the boundaries (shear & normal stress), than the analytic solution. The role that the boundary conditions play in determining the spring constant k should be investigated in detail in future studies. On the other hand, the results for case 2 are numerically very close to one another.

Determining these values is significant because they will affect the pull-in voltage value. Again, by using the analytical formula from the literature, one can calculate the required voltage (volts) to pull the membrane in. Equation 4.16 is given in the fourth section:

$$V_{pull-in} = \sqrt{\frac{8k}{27A\varepsilon_0} g_0^{\,3}}$$

(5.1)

In this equation, the numerical values of the inputs are: the gap between the two electrodes ($g_0 = 1.7 \mu m$), the permittivity of the free space ($\varepsilon_0 = 8.85x10^{-12}$ F/m) and the area of the lower electrode ($A = 80x10^{-10}$ m^2).

By utilizing the strength of materials approximation and FEM simulation results spring constants are calculated. Substituting these values into the Equation 5.1 the pull-in

voltage can be determined for the given material properties and the dimensions of the rectangular shaped switch.

For the spring constant calculated analytically, the pull-in voltages are:

Applied Force type for spring constant	Pull-in Voltage (V_p) (Volts)
Over the entire membrane (Case 1)	12.48
1/3rd of the membrane (Case 2)	9.22

Table 5.2: Pull-in Voltages with the analytical spring constant values.

For the spring constant calculated from ANSYS, FEM Analysis, the pull-in voltages are:

| Applied Force type for spring constant	Pull-in Voltage (V_p) Volts
Over the entire membrane (Case 1)	10.98
1/3rd of the membrane (Case 2)	8.99

Table 5.3: Pull-in Voltages with the ANSYS spring constant values.

From the results above, Table 5.2 and 5.3, again there is a difference between the two pull-in voltages for case 1 (simulated versus analytically calculated). This is again probably because fully 3-D elements were used in the FEM simulation. For case 2, pull-in voltage results are very close.

6 Finite Element Modeling of Membrane Designs

In this section, the models used to simulate RF MEMS Switch behavior are introduced. The switches examined in this section not only have non-rectangular geometries but also wide range of dimensions. Therefore, dimensions of the membranes are given for each specific analysis.

A schematic view of the RF MEMS Switch can be seen in Figure 6.1. The typical switch consists of a movable membrane, two posts which anchor the membrane, lower electrode, dielectric layer and the Si substrate.
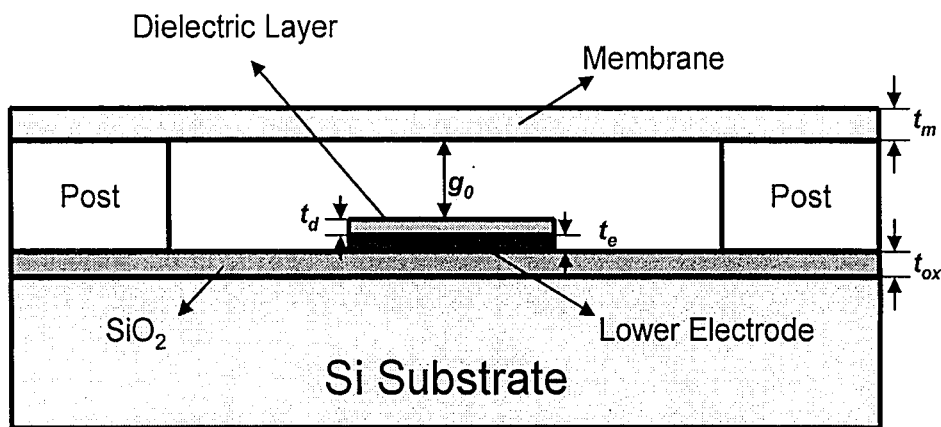
Figure 6.1: Schematic view of the fixed-fixed bridge MEMS Switch.

All electrostatically actuated MEMS switches have similar designs where two electrodes are placed parallel to each other. Membrane designs (movable electrode) can differ for various switch designs. In this study, four different membrane designs are studied. Figure 6.2 shows the different designs of the membranes of interest. These are micrographs of the actual fixed-fixed bridge structure RF MEMS Capacitive Switches tested in the Compound Semiconductor Technology Laboratory at Lehigh University.

(M-1) (M-2) (M-3) (M-4)
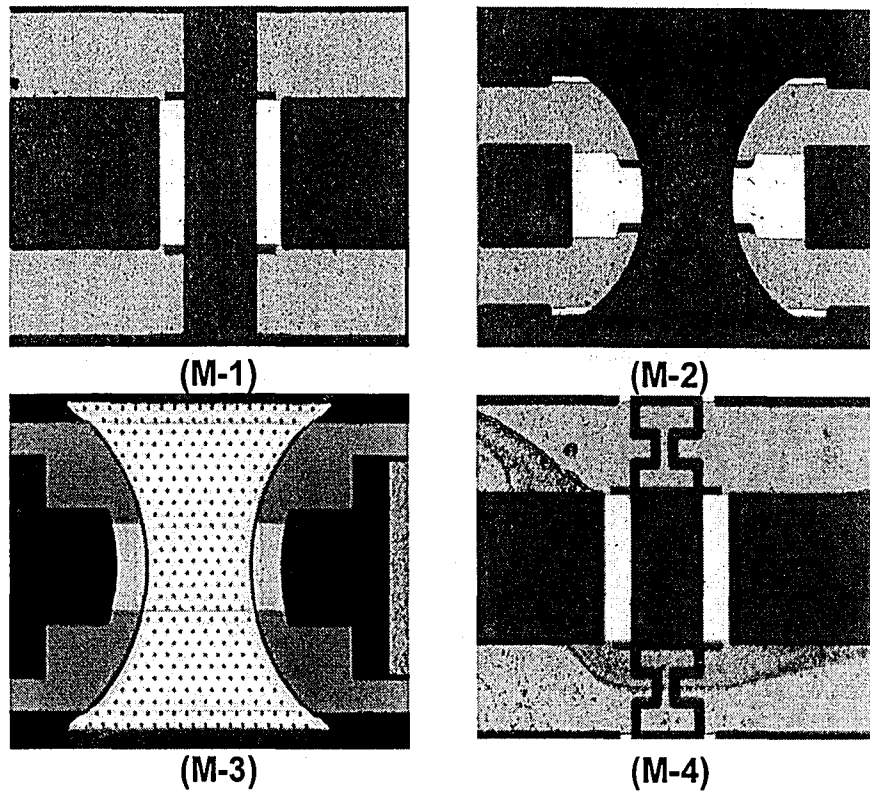
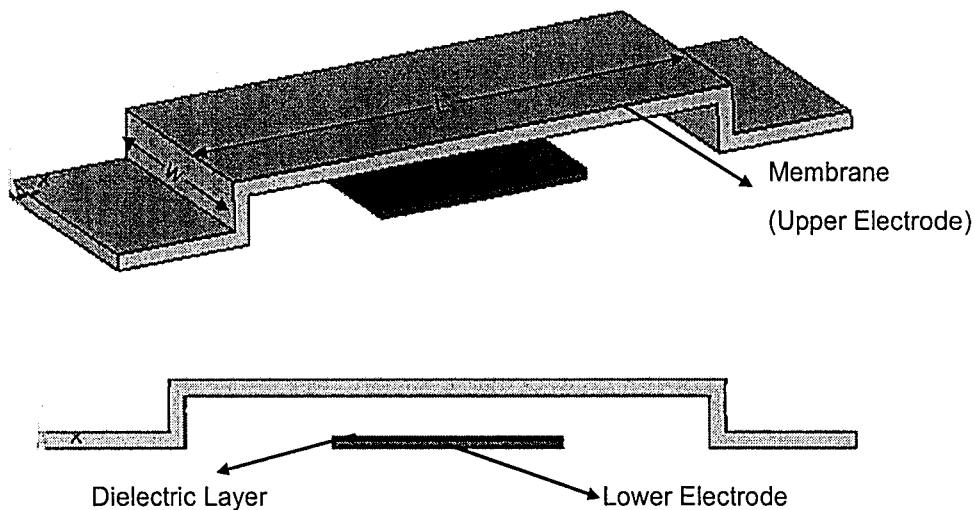**Figure 6.2:** Micrographs of the different membrane designs.

The M-1 is a simple rectangular shape which used earlier in the Section 4 for spring constant calculations. M-4 has a rectangular shape and connected to the sides with spring type arms. M-2 is a "bow-tie" shaped design, and M-3 is another "bow-tie" shaped design with circular holes. Holes in the MEMS switches are primarily a processing artifact, used to aid in release of the membrane during etching. All finite element models are created in the ANSYS preprocessing software.

For the structural analysis SOLID95 ASNYS elements, twenty-noded structural hexahedron elements were used and for the electrical part, SOLID123, ten-noded tetrahedral elements are used. Also note that, in the model that has been used for electromechanical analysis, a total of 51000 electrical and mechanical elements were used. Because the dimensions are very small ($\sim \times 10^{-6}$m), the μMKS unit system is used to

create finite element models of the MEMS structures. This allows easier meshing of the structures with sufficient figures for nodal coordinates. However, because the difference between the membrane thickness and its length is very large meshing has to be done with smaller elements to prevent highly distorted elements, making the computing time longer.

Another schematic view of the switch can be seen in Figure 6.3. In this illustration, posts, which hold the membrane in the air, are also made out of membrane material. Since the interest is to investigate different designs of membranes, posts are not created in any of the models used for analysis. Only for the electrostatic simulation, lower electrode and the dielectric layer included in the finite element model.

Figure 6.3: Schematic diagram fixed-fixed bridge Switch with posts made out of membrane material.

Membranes are created in two parts in order to have a straight line of nodes on the plane of symmetry, thus allowing for the results to be obtained exactly on the symmetry plane. This aids in plotting of the necessary graphs. Figure 6.4 shows the meshed membranes. As mentioned earlier, in order to be able to investigate the effect holes play in the

create finite element models of the MEMS structures. This allows easier meshing of the structures with sufficient figures for nodal coordinates. However, because the difference between the membrane thickness and its length is very large meshing has to be done with smaller elements to prevent highly distorted elements, making the computing time longer.

Another schematic view of the switch can be seen in Figure 6.3. In this illustration, posts, which hold the membrane in the air, are also made out of membrane material. Since the interest is to investigate different designs of membranes, posts are not created in any of the models used for analysis. Only for the electrostatic simulation, lower electrode and the dielectric layer included in the finite element model.
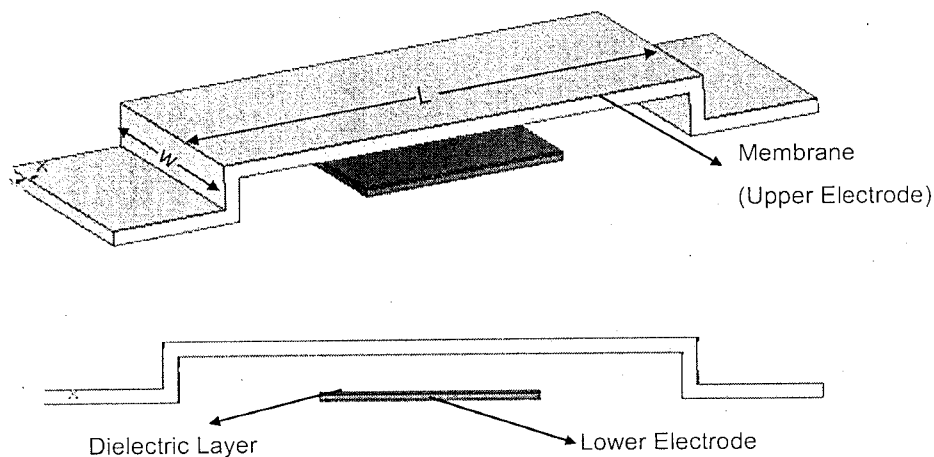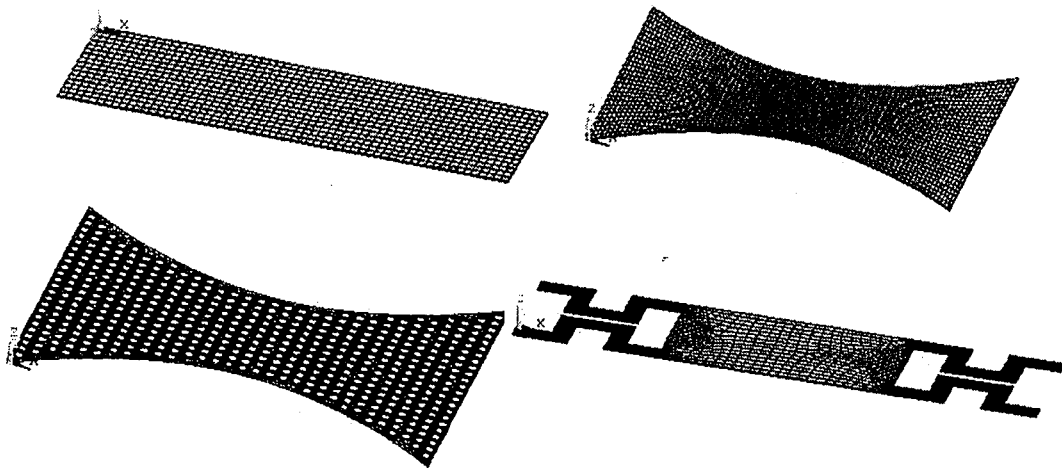

Figure 6.3: Schematic diagram fixed-fixed bridge Switch with posts made out of membrane material.

Membranes are created in two parts in order to have a straight line of nodes on the plane of symmetry, thus allowing for the results to be obtained exactly on the symmetry plane. This aids in plotting of the necessary graphs. Figure 6.4 shows the meshed membranes. As mentioned earlier, in order to be able to investigate the effect holes play in the

membrane behavior, M-3 has an ordered array of (~400) honeycomb shaped holes. These holes can be seen in a closer view, in Figure 6.5. This particular design, M-3, is meshed with shell elements. Detailed explanation of M-3 will be given in Section 8 (Modal Analysis Section). Other than M-3, all the finite element models have 2 elements through the thickness, unless otherwise noted.

Figure 6.4: FE Models of M-1, M-2, M-3 and M-4.

Figure 6.5: Zoomed in view of the M-3.

There are a couple different ways to solve electromechanical coupled analysis in ANSYS and one of them is filling the space between the electrodes with an air mesh which allows solution for the electrostatic forces. Therefore an air volume was created enveloping the entire switch system and meshed with SOLID123 ten-noded tetrahedral elements (~30000 elements). Figure 6.6 shows the entire model with a transparent "air"

39

membrane behavior, M-3 has an ordered array of (~400) honeycomb shaped holes. These holes can be seen in a closer view, in Figure 6.5. This particular design, M-3, is meshed with shell elements. Detailed explanation of M-3 will be given in Section 8 (Modal Analysis Section). Other than M-3, all the finite element models have 2 elements through the thickness, unless otherwise noted.
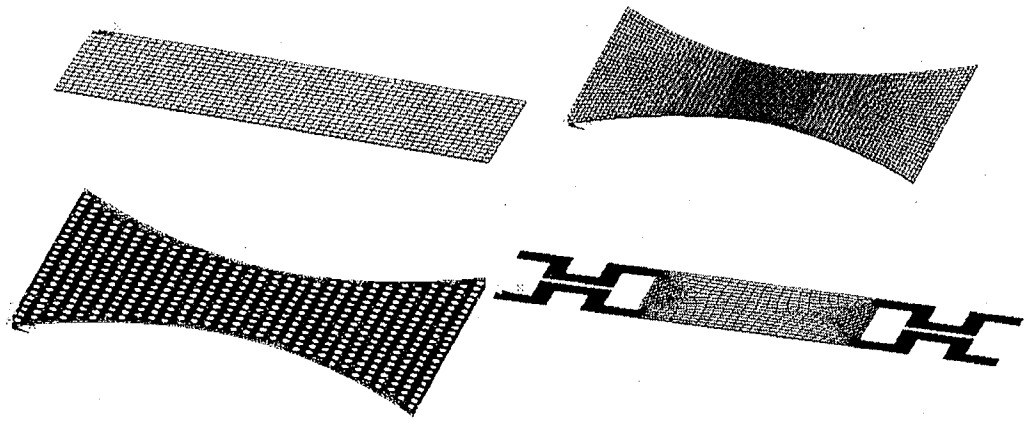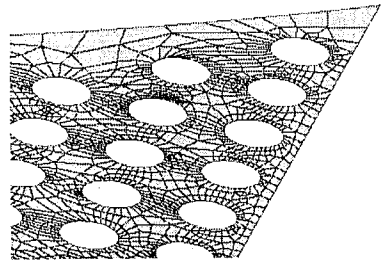

Figure 6.4: FE Models of M-1, M-2, M-3 and M-4.

Figure 6.5: Zoomed in view of the M-3.

, There are a couple different ways to solve electromechanical coupled analysis in ANSYS and one of them is filling the space between the electrodes with an air mesh which allows solution for the electrostatic forces. Therefore an air volume was created enveloping the entire switch system and meshed with SOLID123 ten-noded tetrahedral elements (~30000 elements). Figure 6.6 shows the entire model with a transparent "air"

volume. In this model, the membrane and the lower electrode material is gold (Au) and the dielectric layer is silicon dioxide.

Figure 6.6: Created volumes for the complete switch with lower electrode, dielectric layer and the air volume.

Figure 6.7: FE Models for (a) membrane, lower electrode and dielectric layer and (b) the "air" mesh.

Figure 6.7 shows the finite element models of (a) the membrane, lower electrode with the dielectric layer and (b) the "air" mesh. The entire system has ~51000 elements. In this model, the membrane lower electrode and the dielectric layer have 1 element through the thickness. In the next section, Section 7, the coupled analysis will be explained in detail.

volume. In this model, the membrane and the lower electrode material is gold (Au) and the dielectric layer is silicon dioxide.
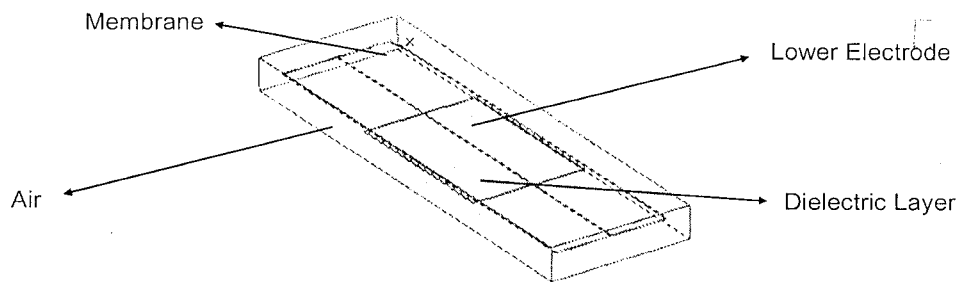

Figure 6.6: Created volumes for the complete switch with lower electrode, dielectric layer and the air volume.
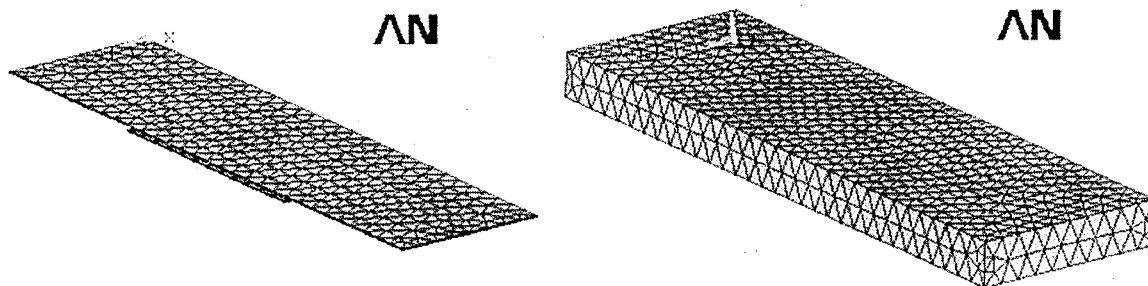

Figure 6.7: FE Models for (a) membrane, lower electrode and dielectric layer and (b) the "air" mesh.

Figure 6.7 shows the finite element models of (a) the membrane, lower electrode with the dielectric layer and (b) the "air" mesh. The entire system has ~51000 elements. In this model, the membrane lower electrode and the dielectric layer have 1 element through the thickness. In the next section, Section 7, the coupled analysis will be explained in detail.

7 Electromechanically Coupled Rectangular Switch Model

In this section, results are given for the complete electrostatically actuated switch using ANSYS. Realistic electrical conditions are considered in this simulation. Coupled field analysis is a combination of analyses from electrostatics and mechanical modeling that interact to solve the global interdisciplinary engineering problem. MEMS require interdisciplinary modeling that involves both mechanical and electrical interaction. In these types of analyses, the electrostatic solution serves as input for the mechanical model and vice versa. ANSYS provides several different ways of solving these types of coupled problems, known as the direct method and the sequential method. In the direct method, ANSYS has appropriate elements which are specific for coupled fields that take care of the coupling. By utilizing this data in one solution, coupling can be successfully done. In the other case, known as the sequential method, different fields need to be introduced in different physics files and then solved. In this method, coupling of the two fields is done by applying the results from one to the other as the loads. In this study, sequential coupled analysis is performed and the two different physics files are created for the structural part and for the electrical part. Since the voltage values are controlled, the results from the electrical field are used as loads in the structural field. More specifically, the electrostatic forces are created by applying voltage differences to the electrodes. Then, those forces are used in the structural analysis as the loads applied to the deformed electrode. In this specific analysis, volumetric air mesh is used to complete the electrostatic fields and forces.

The MEMS switch model dimensions used in the example calculations are: L (bridge length) = 300 μm, b (membrane width) = 80 μm, t_m (membrane thickness) = 1 μm, g_o (gap height) = 1.7 μm, W (lower electrode width) = 80 μm, t_e (lower electrode thickness) = 0.8 μm, and t_d (dielectric layer thickness) = 0.15 μm, (see Figure 7.1). Both the membrane electrode and the lower electrode are gold, which has a Young's Modulus of $E=78Gpa$, a Poisson's ratio of $(v=0.44)$ and a density of $(d=19300kg/m^3)$. The dielectric layer material (SiO_2) has a Young's Modulus of $E=75Gpa$, a Poisson's ratio of $(v=0.17)$, a density of $(d=2200kg/m^3)$, and the relative permittivity of $(\varepsilon_r = 3.78)$. And for the air relative permittivity of 1 is used (considered as in vacuum). For comparison purposes, just the rectangular membrane is used in this simulation.

Figure 7.1 shows the membrane, the lower electrode and the dielectric layer from the corner of the lower electrode in a zoomed-in view. Figure 7.2 shows the complete system in a transparent view depicting the boundaries of the air mesh covering the entire system.

The membrane is created in two parts, as can be seen in Figure 7.1. The straight line is along the plane of symmetry in order to be able to get the nodal results smoothly plotted along the membrane's symmetry plane after each applied voltage step. Because the actual dimensions are quite small, the μMKS unit system is used. Thus, the meshing must be done carefully.

The switch system – the membrane, lower electrode, dielectric layer and the air mesh, is created and meshed (mesh shown in Figure 6.7). The two physics files are used one after the other iteratively to determine the displacements for an input voltage value. These files are named 'STRUCTURE' and 'ELECTROS' in order to be able to use the

commend ESSOLV in ANSYS, which performs the electrostatic-structural analysis. The ESSOLV calls an ANSYS macro, which automatically performs a coupled electrostatic-structural analysis using the iterative approach. During the solution, it displays the periodic updates of the convergence.
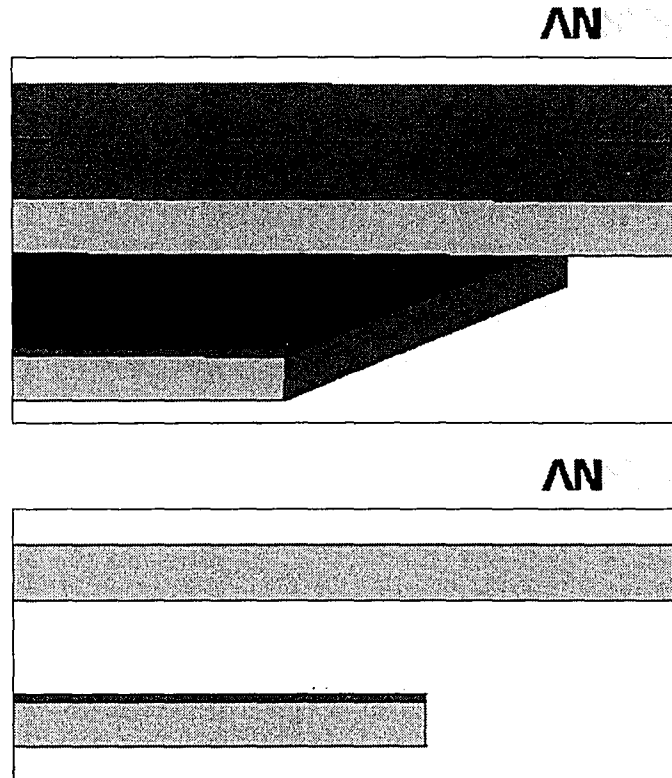
Figure 7.1: Lower electrode, membrane and the dielectric layer (color coded for different materials).
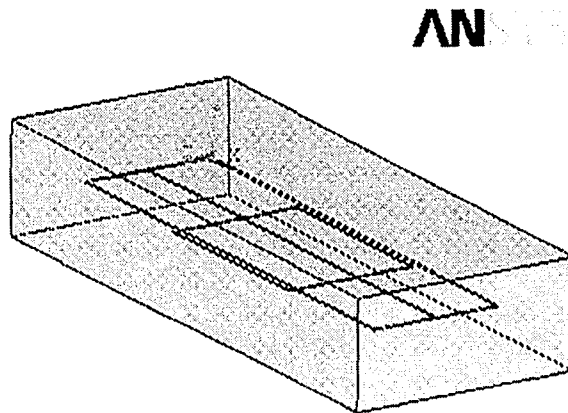
Figure 7.2: Transparent view of the entire system.

The "air" mesh is created as a rectangular "box". For the first trial; the dimensions were (~80µm x 360µm x 140µm). The capacitive switch system is centered in the middle of the rectangular "box". Calculations were carried out for larger/smaller dimensions of the "air" mesh. There was roughly a 5% change in the results when smaller dimensions were used for the "air" mesh; however, there was essentially no change when larger dimensions were used. Therefore, for all of the simulation results presented here, the (~80µm x 360µm x 140µm) rectangular "box" is used as the "air" mesh.

In actual operation, the capacitive switch touches to the dielectric layer between the electrodes while it is in the 'ON' position. In order to prevent interpenetration while is in the down position, contact elements need to be used. In ANSYS (for contact problems), elements have to be created on both surfaces facing each other, so that contact can be simulated. CONTA174, which is used to represent contact between surfaces for 3D analysis, is used on the lower area of the membrane. Also, to meet with the contact elements when the membrane comes down, target elements need to be placed on the upper surface of the dielectric layer. The TARGE170 elements, which are compatible with CONTA174 elements, are used on the dielectric layer surface. Figure 7.3 shows normal vectors that identify target elements on the surfaces with the membrane, dielectric layer set.
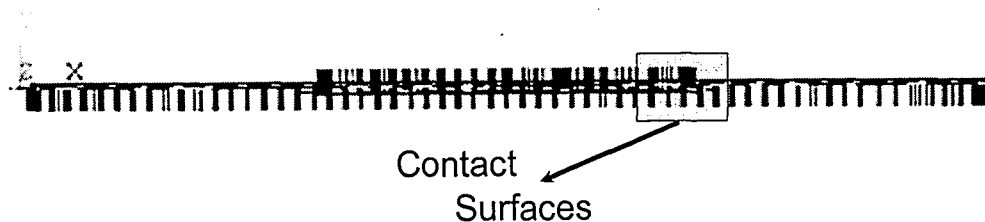
Figure 7.3: Contact and target elements facing each other on the lower area of the membrane and the surface of the dielectric layer.

44
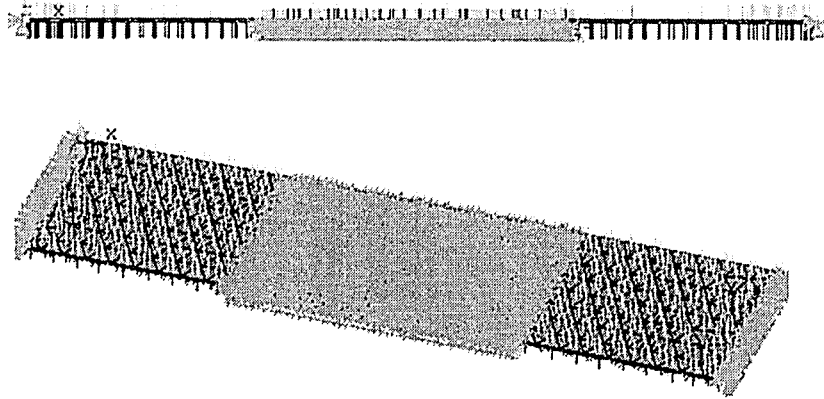
Figure 7.4: Applied voltage in yellow, the contact and the target elements are in blue.

Figure 7.4 also shows the applied voltage (depicted with yellow colored arrows) and the contact elements on the electrode surfaces (blue arrows). A static solution is performed for a given voltage value. ESSOLV solves the coupled electrostatic-structural problems automatically, as explained earlier. It also detects the air structure interface and applies a Maxwell surface flag on the electrostatic elements. This flag is used to initiate the transfer of forces from the electrostatic region to the structure [23].

The applied voltage values used in this study were 4, 8, 12 and 12.8 Volts. The pull-in voltage is found to be 12.8 Volts for this specific example switch with the rectangular shaped membrane. Figure 7.5 shows the deformed membrane profiles in cross section at different applied for the nodal values taken from the symmetry axis.
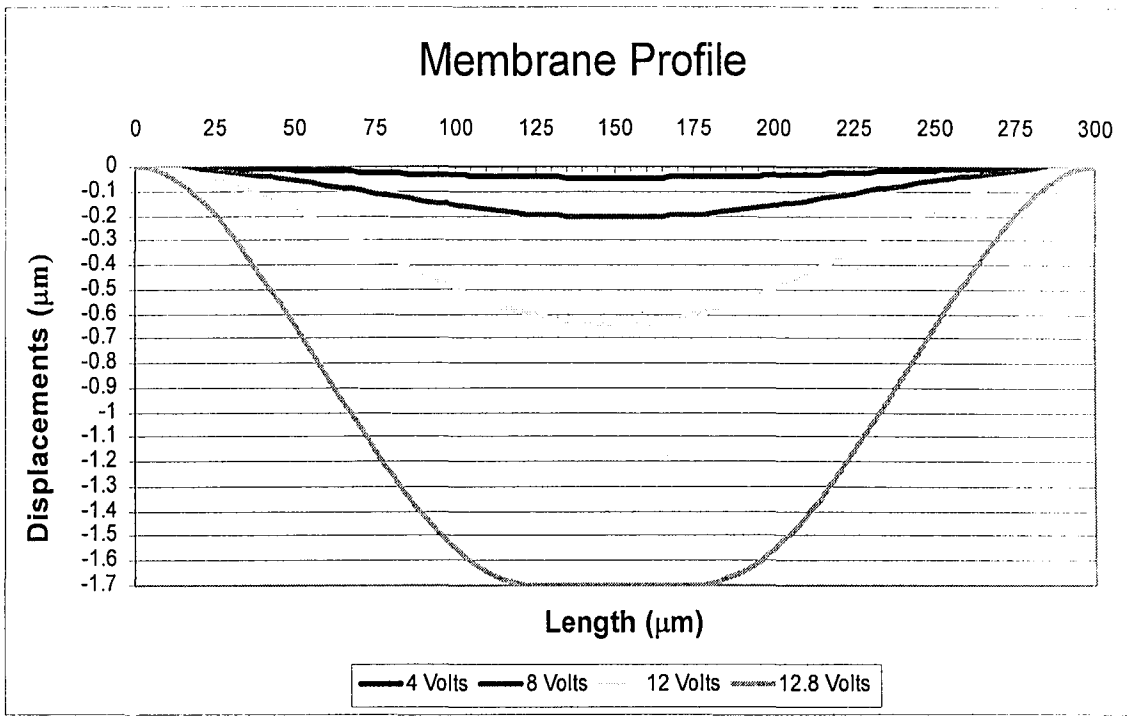
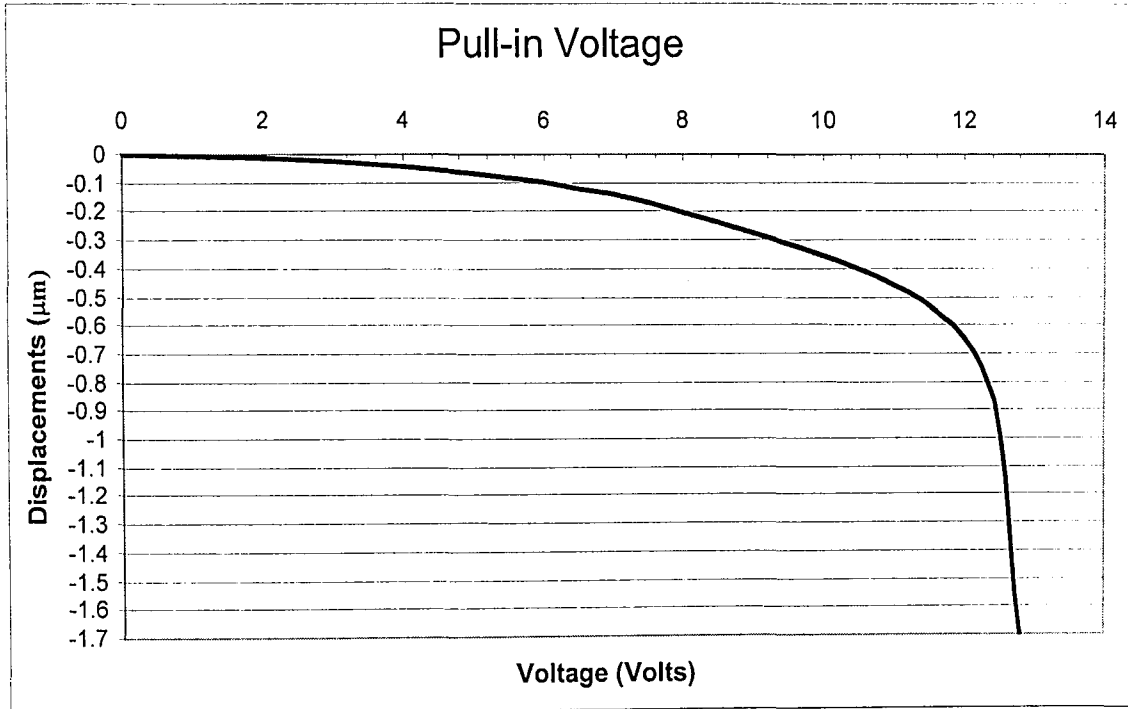**Figure 7.5:** Membrane profile as a function of the applied voltage.

Figure 7.6: Pull-in Voltage versus centerline displacement.

46

The problem is solved iteratively for every input voltage value and the maximum displacement is determined from the analysis. Any initial stresses, from the manufacturing process were not included in the simulation. Therefore, the pull-in voltage determined from the finite element simulation is lower than the voltage obtained from experimental measurements. The voltage versus vertical displacement graph can be seen in Figure 7.6. The results match quite well with pull-in voltage graphs found elsewhere in the literature.

It should be noted that the ESSOLV command also provides the user with the potential energy for each applied voltage value. This is useful for calculating the capacitance versus voltage values. From reference [24], the energy stored in a capacitor can be expressed in terms of the work done by the voltage difference, where the voltage represents energy per unit charge. Therefore, the work to move a charged element from point A to point B is equal to Vdq. In such a case, the voltage is proportional to the amount of the charge already on the capacitor. If Q is the total amount of charge stored when the voltage difference is applied, the stored energy is given by the integral:

$$U = \int_0^Q \frac{q}{C} dq = \frac{1}{2} \frac{Q^2}{C} \tag{7.1}$$

where, U is the energy, V is the voltage and q is the charge. Knowing that the capacitance, $C = \frac{Q}{V}$, U can be written as:

$$U = \frac{1}{2} \frac{Q^2}{C} = \frac{1}{2} QV = \frac{1}{2} CV^2 \tag{7.2}$$

which leads to the capacitance equation in terms of potential energy:

$$C = \frac{2U}{V^2} \tag{7.3}$$

47

By utilizing Equation 7.3 and the potential energy output from ANSYS, the capacitance versus applied voltage graph is plotted in Figure 7.7.
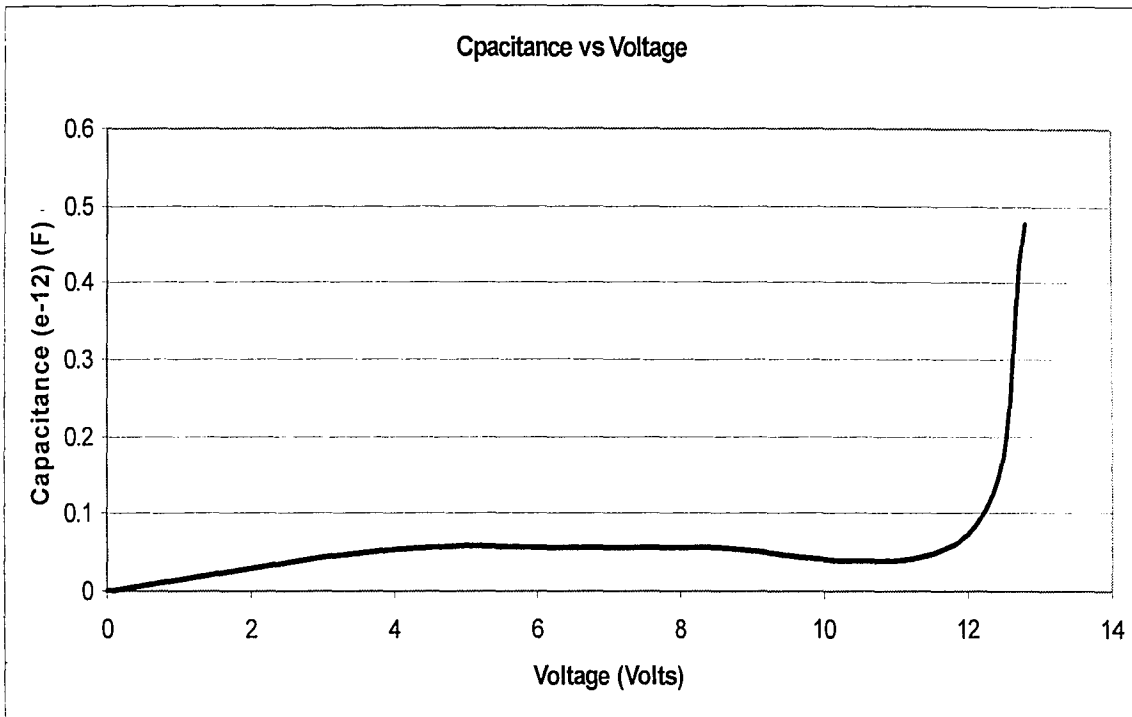
Figure 7.7: Capacitance calculated versus voltage graph

Because the ESSOLV command provides the results for both the electrostatic and for the structural models, it is possible to generate contour plots of electrical field and the potential energy distribution for the applied voltage values. Figure 7.8 shows the potential energy as viewed from the outside of the air volume "box" for an applied voltage of 4 Volts.
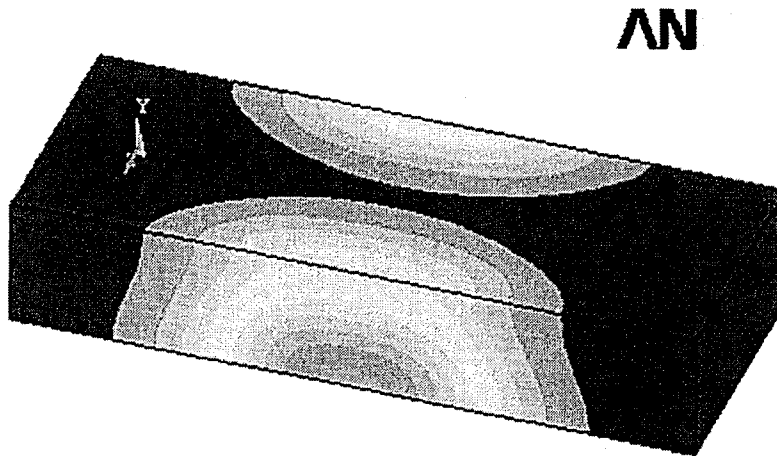
Figure 7.8: Potential energy contour plots from outside of the air mesh "box".

A more useful plot shows the potential energy plotted on symmetry plane, parallel to the y axis. Figure 7.9 and Figure 7.10 show the potential energy contours for 4 Volts.
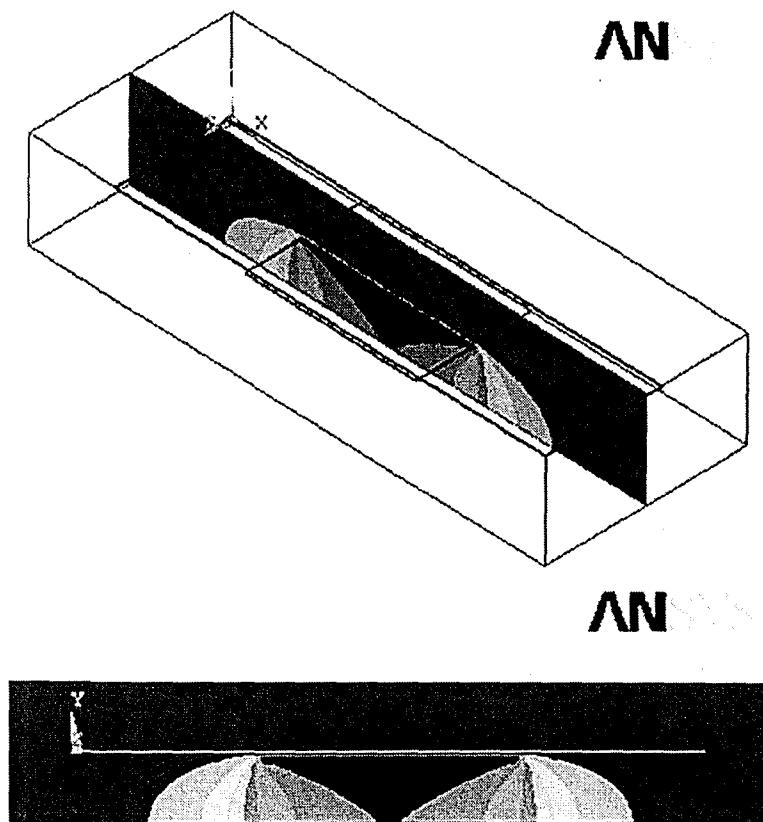
Figure 7.9: Symmetry surface for a slice through the middle of the membrane showing the potential energy contours.

49
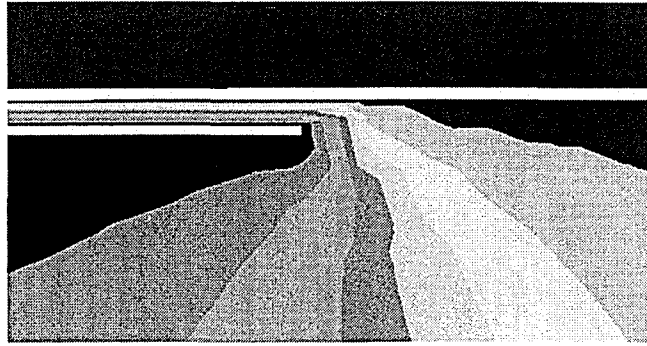
Figure 7.10: Zoomed-in view of one of the corners close to the dielectric layer.

The electric field, a vector quantity is shown in Figure 7.11 and Figure 7.12 for an applied voltage of 8 Volts.
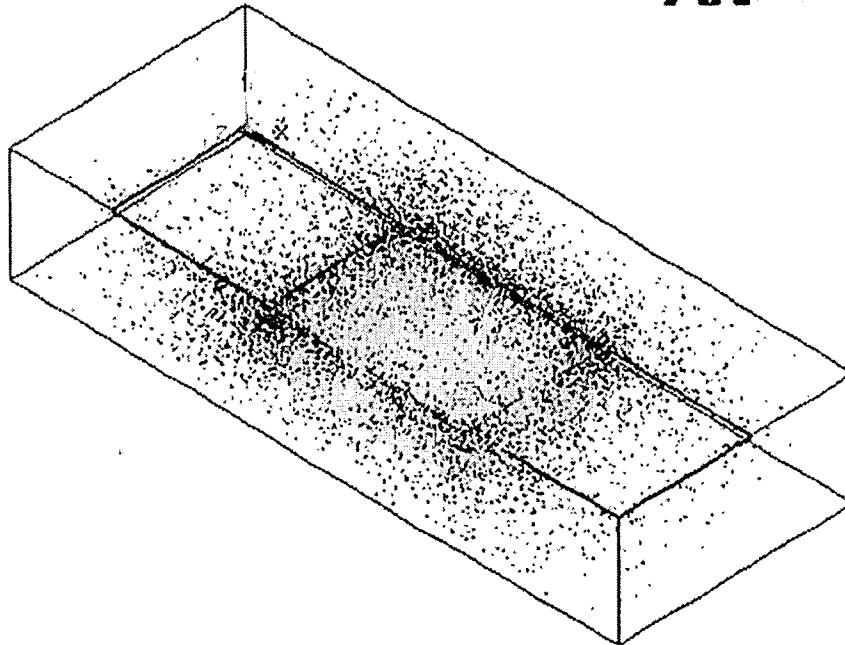
Figure 7.11: Vectors show the electric field between the two electrodes. Yellow color represents the highest filed values (accumulated where two electrodes are facing each other).
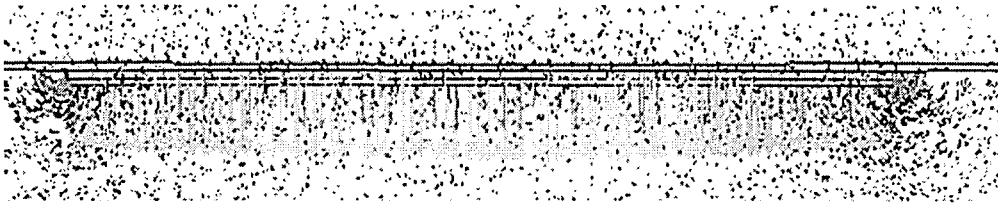
Figure 7.12: Zoomed-in view of the membrane and the lower electrode showing electric field vectors.

Figure 7.13 shows the same vectors on a black background in a zoomed-in view on the right lower electrode/dielectric boundary. As it can be seen from the figure, the field vectors are perpendicular to the electrodes in the middle, and "fringe" close to the electrode's free surface.
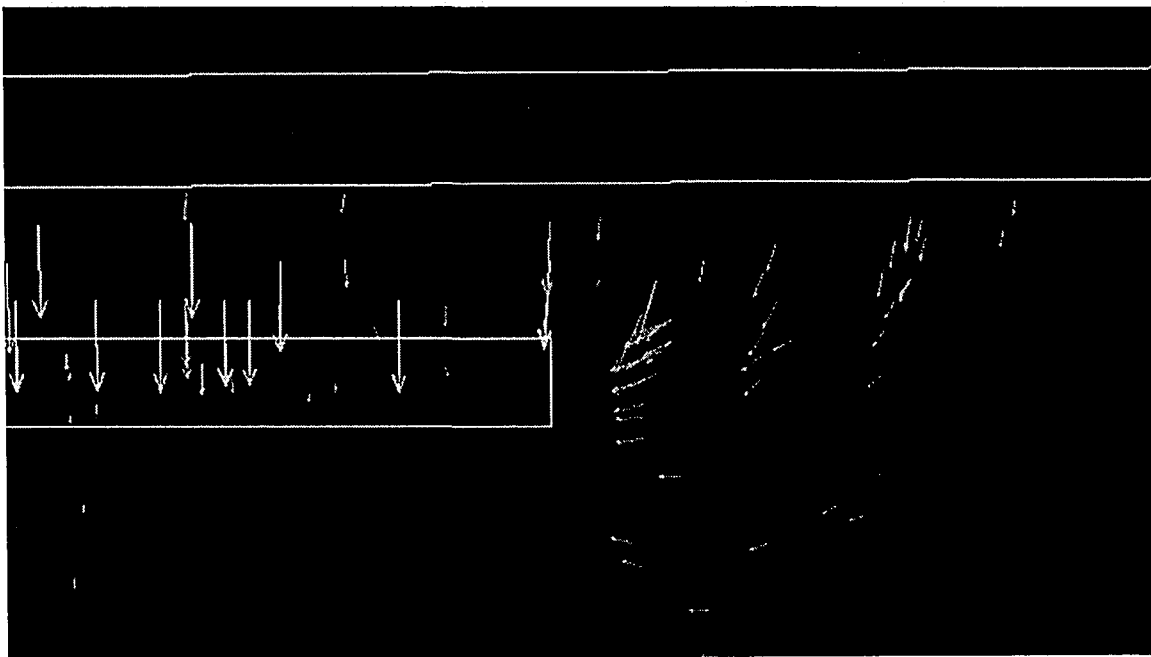
Figure 7.13: Zoomed-in view of the membrane and the lower electrode.

8 Modal Frequencies

In this section, only the mechanical membrane FE models are used since the electrostatics has no bearing on the resonant frequency. Resonance occurs when the vibration frequency reaches the natural frequency which may damage the switch. Thus, investigating the mechanical resonance behavior of the switches can be important for reliability issues. Natural frequencies can also be used to extract the residual stress in the membrane [25]. This study was performed to aid the experimental measurements made at the Compound Semiconductor Technology Laboratory at Lehigh University precisely for this purpose. The membrane models used in this section are: a bow tie shaped $0.3\mu m$ thick aluminum with the dimensions of L (bridge length) = 310 μm and w (membrane width) = 120-250 μm; another bow-tie shaped membrane with the same dimensions, but perforated with a honeycomb pattern of holes. The hole diam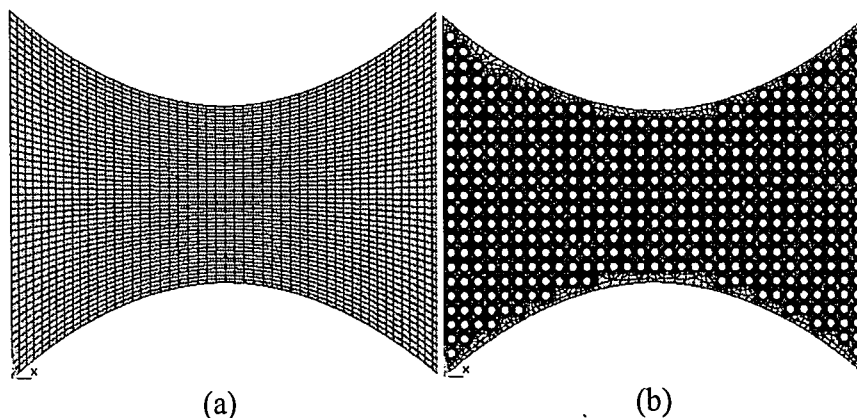eter is $7\mu m$ and center-center spacing is $12\mu m$. The initial stress effect is included in the finite element models. Figure 8.1 shows the finite element models.

(a)   (b)

Figure 8.1: Finite element models of two "bow-tie" shaped membrane designs (a) without the holes and (b) with the holes.

Since the thickness of the membranes is considerably smaller when compared with its length and width, 8-node structural SHELL93 elements are used to mesh the FE

models. FE model (a) has 2500 elements and (b) has 35000 elements. As can be seen in Figure 8.1, it was very difficult to mesh the model with the holes and thus, required long computing times. The boundary conditions for the membranes are simply that both ends of the membrane are fixed in the X and Y directions. The primary interest was the first modal frequency; however, to investigate the other mode shapes, a simulation is performed for the first four modes. Table 8.1 shows the natural frequencies of the "bow tie" membranes without initial stress.

Bow-tie (Sigma=0MPa)	
	Frequency (Hz)
With the Holes	16,801
Without the Holes	19,256

Table 8.1: Natural frequencies without the initial stress effect.

In order to include the initial stress effects, the desired stress value simply introduced into ANSYS by applying a temperature difference, ΔT. The value of ΔT used was determined by the formula $\sigma_0 = -E\alpha\Delta T$. ($E$ is the Young's modulus and α is the Thermal Coefficient of the material). Then, a static solution is performed to determine the initial stress distribution. Figure 8.2 shows the generated stress contours on a "bow tie" shaped membrane.
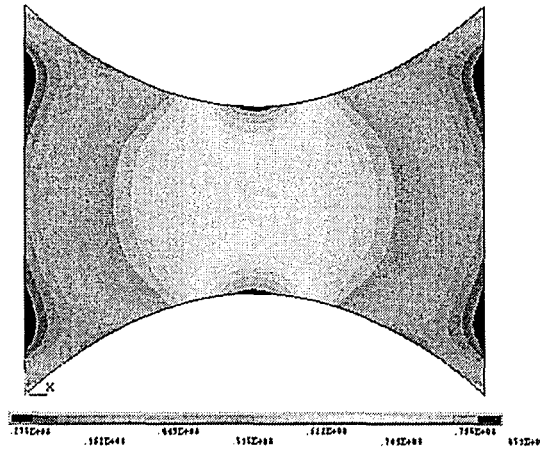
Figure 8.2: Stress contours in the membrane.

As can be seen from Figure 8.2, the desired stress was 50MPa, due to the geometry; final stress distribution on the membrane was not uniform everywhere and varied between (30MPa-70MPa) with $\sigma_0 = 50MPa$. This stressed membrane is subsequently used in the modal analysis to determine the natural frequencies. Table 8.2 shows the natural frequencies for both membrane designs including the initial stress effect.

Bow-tie (Sigma=50MPa)	
	Frequency (Hz)
With the Holes	**211,949**
Without the Holes	**252,890**

Table 8.2: Natural frequencies with the initial stress effect.

As can be seen from both Table 8.1 and Table 8.2, there is a significant increase in the natural frequencies due to the initial stress in the membrane. The stress in the membrane not only increases the frequency but also increases the pull-in voltage.

Note, that the membrane with the holes has 35000 elements as oppose to 2500 elements in the solid membrane. Therefore, to simplify the geometry and to reduce the

54

computing time, the ratio of mass between the two bow-tie shaped membrane designs (the bow-tie with holes and the bow-tie without the holes), is used to determine an effective Young's modulus, $E_{\text{eff}} = (m_{\text{holes}} / m_{\text{solid}})E$. The effective Young's modulus and the solid "bow-tie" FE model are both used to determine the natural frequency of the perforated "bow-tie" membrane. The results were found to be identical. It should also be noted that all of the mechanical resonance calculations are performed without considering any damping effects.

The natural frequencies and associated are shown in Figure 8.3 for the first 4 modes of various membrane designs tested at the Lehigh University Laboratories.

| $f_1 = 19712$ Hz | $f_2 = 38247$ Hz | $f_3 = 50835$ Hz | $f_4 = 73318$ Hz |

| $f_1 = 28141$ Hz | $f_2 = 49036$ Hz | $f_3 = 71454$ Hz | $f_4 = 93061$ Hz |

| $f_1 = 4715$ Hz | $f_2 = 6762$ Hz | $f_3 = 11575$ Hz | $f_4 = 29741$ Hz |
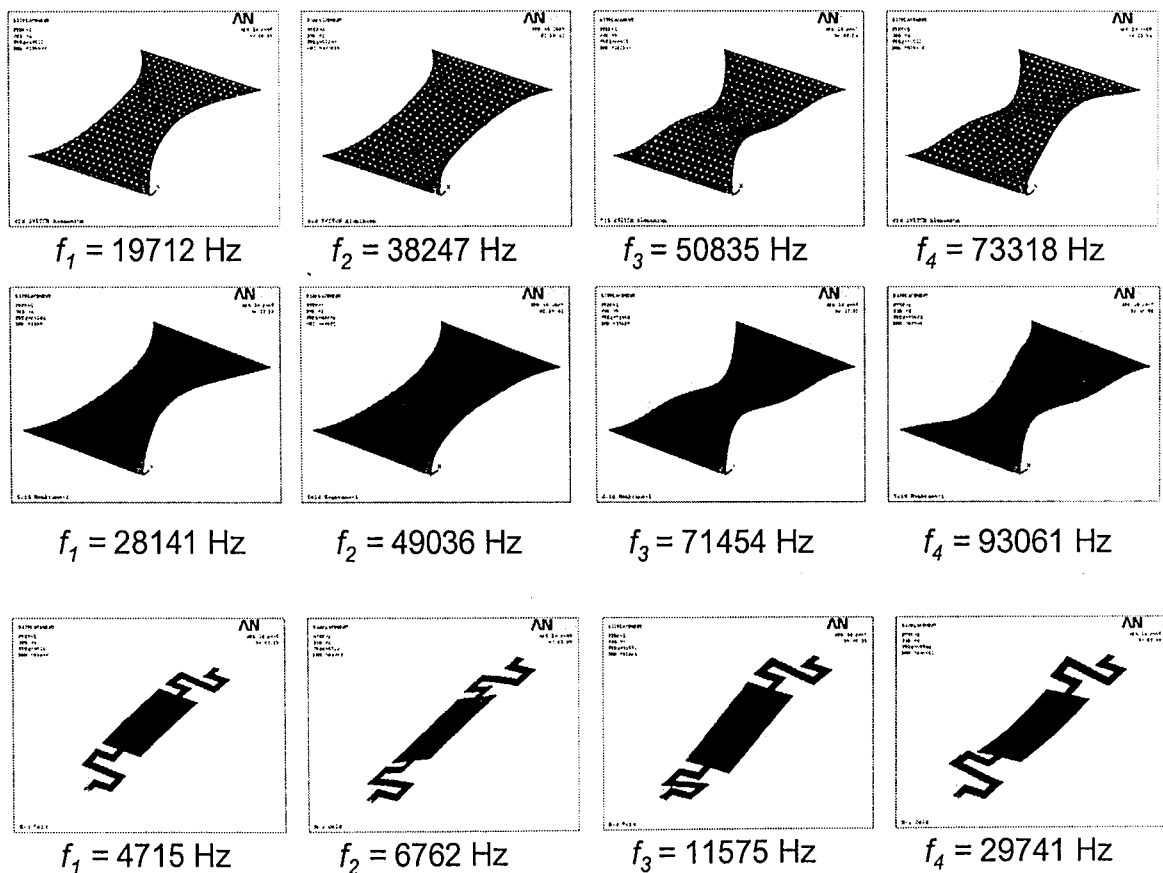
Figure 8.3: First four modal shapes for various membrane designs.

$f_1 = 7743$ Hz $f_2 = 14838$ Hz $f_3 = 21480$ Hz $f_4 = 45418$ Hz

$f_1 = 4261$ Hz $f_2 = 6299$ Hz $f_3 = 10690$ Hz $f_4 = 18091$ Hz

$f_1 = 11873$ Hz $f_2 = 29723$Hz $f_3 = 32694$ Hz $f_4 = 63077$ Hz
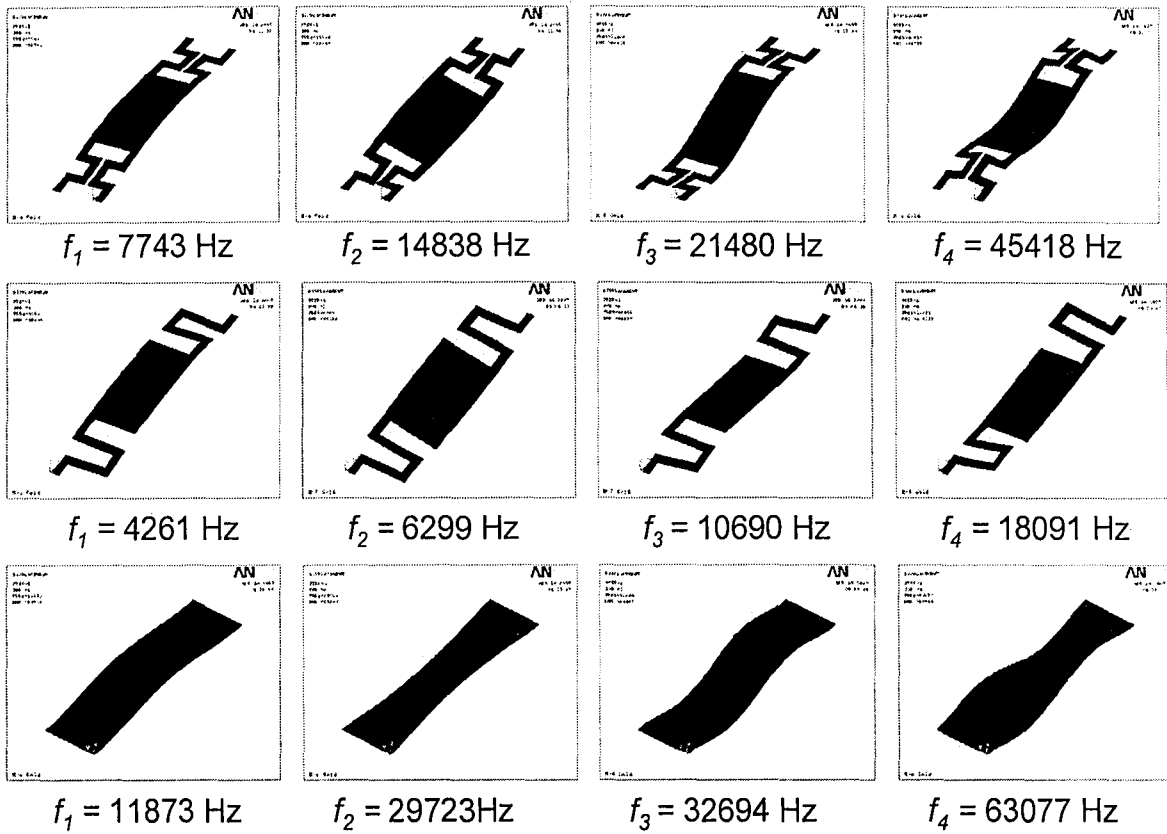
Figure 8.4: First four modal shapes for various membrane designs.

9 Viscoelastic Behavior

The purpose of this section is to examine the time dependent material behavior of capacitive switches. To be able do this, instead of determining the electrostatic force needed to pull down the membrane for an applied voltage, the displacements are directly specified on the portion of the membrane that is known to come into contact with the lower electrode. This provides a simplified model for observing the viscoelastic material behavior of the switching mechanism. The results were generated for different hold and recovery times. As expected, the membrane recovers the elastic portion of its deformation immediately after the displacement constraints are removed, but takes a finite amount of time to recover the remaining viscoelastic strain.

Figure 9.1 contains a plot of the uniaxial stress relaxation data for the Au membrane material examined in this study. A four term exponential curve fit (Prony series) provides the necessary material constants for viscoelastic input in ANSYS.
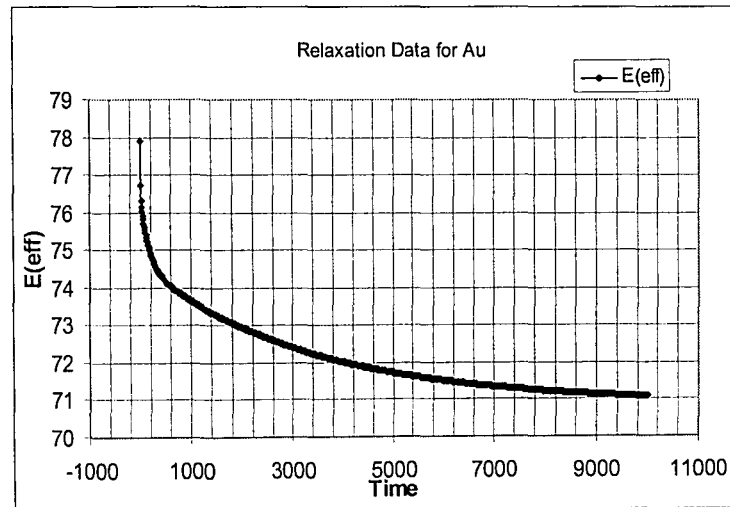

Figure 9.1: Stress Relaxation Data for Au (Courtesy of Professor R. P. Vinci –Lehigh University)

$$E(t) = 70.888 + 3.7326e^{\left(\frac{-t}{3367.6}\right)} + 1.8563e^{\left(\frac{-t}{151.71}\right)} + 0.71619e^{\left(\frac{-t}{7.4307}\right)} + 0.71619e^{\left(\frac{-t}{7.3974}\right)} \quad (9.1)$$

57

In this section, a simple rectangular shape membrane is considered. The dimensions of the membrane used are: L (bridge length) = 300 μm, b (membrane width) = 80 μm, tm (membrane thickness) = 2 μm. The boundary conditions for the mesh shown in Figure 9.2 are simply that both ends of the membrane are fixed in the X and Y directions. The transient analysis is initiated by rapidly displacing the central region of the membrane switch downwards until it reaches its final displaced position on the dielectric layer. During the holding time period, the time increment is determined automatically by ANSYS. However, in an effort to obtain accurate data during the relaxation period, a time increment of 0.1s is specified.

For the purposes of this study, it is assumed that when the membrane switch is closed, the membrane uniformly contacts the entire lower electrode surface. Thus, in the current FEM model, an area is specified in the middle part of the membrane that is subjected to the required displacements. Knowing that the gap between the membrane and the lower electrode is 1.5 μm, this displacement is uniformly obtained in the first second. Then, for the next 60 seconds, the membrane is held in the ON position. After the 60 seconds, the displacements are removed and 60 more seconds are allowed to elapse in order to simulate the material's viscoelastic recovery.
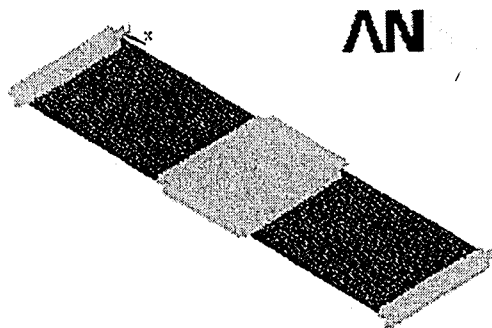
Figure 9.2: FE Model of the membrane with applied displacements.

Figure 9.3 shows the Time versus y-displacement for the area of the membrane with specified displacements. As can be seen from the graph, the membrane is held down for 60 seconds, then upon removal of the specified displacements, the material almost immediately recovers elastically. In the second part of the graph (figure 9.4), which can be seen better in a smaller scale, the relaxation curve of the material slowly goes to zero as a function of time over time as expected.
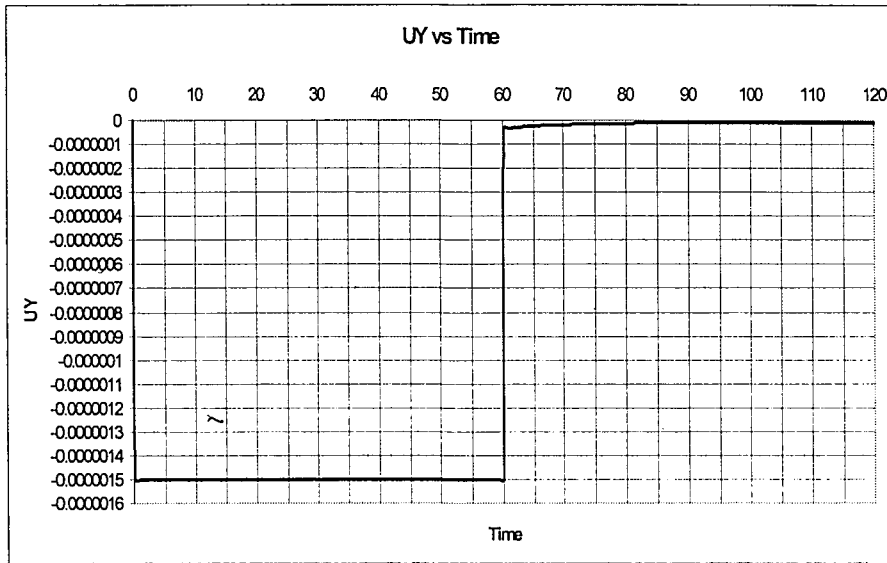
Figure 9.3: The displacement of the specified area of the membrane over time
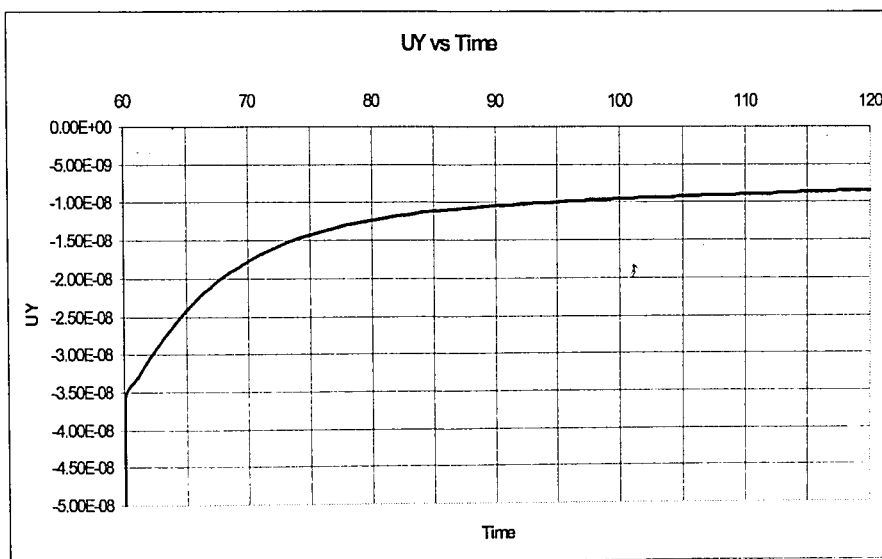
Figure 9.4: The displacement of the specified area of the membrane right after the displacements are removed.

Figure 9.5 shows the results obtained for four different displacement hold times, plotted only for the relaxation time period, (i.e., the last 60 seconds), in order to see the curves in a smaller scale. From the graph, it can be seen that all of the curves exhibit the same time dependent behavior, but their starting point, which is the m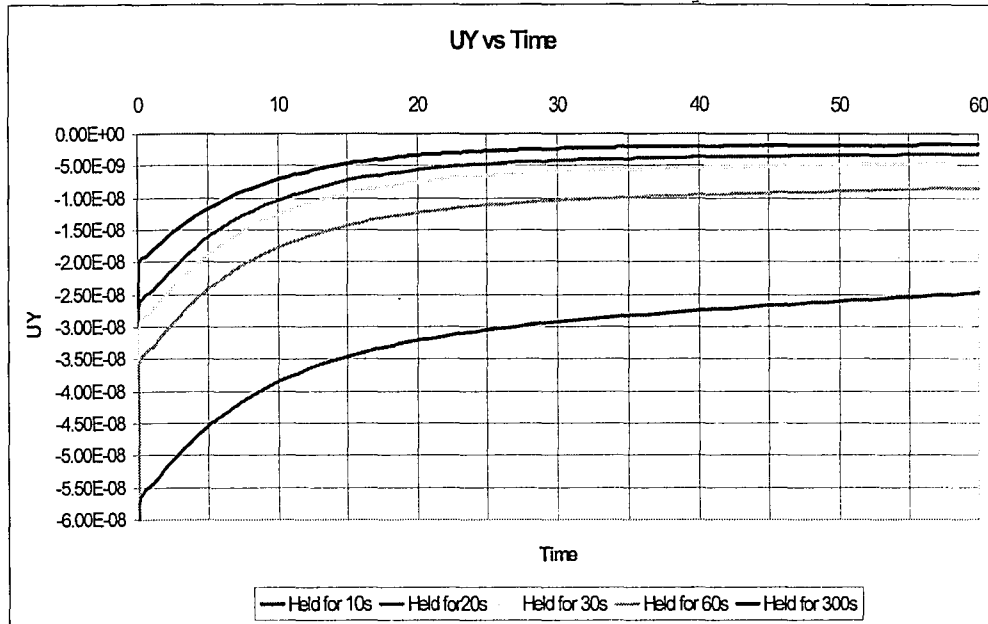aterial's elastic recovery value, differs for various hold times. As the membrane is held for longer times, the elastic recovery gets smaller.

Figure 9.5: Relaxation behavior (60 seconds) for different hold times.

Figure 9.6 shows the results from a cyclic analysis where the switch is displaced and held for 10 second intervals. Again, this figure is also plotted just for the second (relaxation) part of the solution, to be able to see the curves better in the smaller scale. As can be seen in the figure, after 60 seconds of hold time, the membrane recovers its elastic deformation almost immediately. Ten more seconds of viscoelastic recovery are permitted, before returning the switch to its deformed (down) position, where it is again held for 10 seconds. This process was repeated four times, as shown in the Figure 8.6.

From this figure, one can observe that, if the membrane is placed in the down position before it completely recovers all of its time dependent displacement, this will affect its subsequent elastic recovery and the membrane will not be able to recover the same amount of Y displacement in successive cycles.
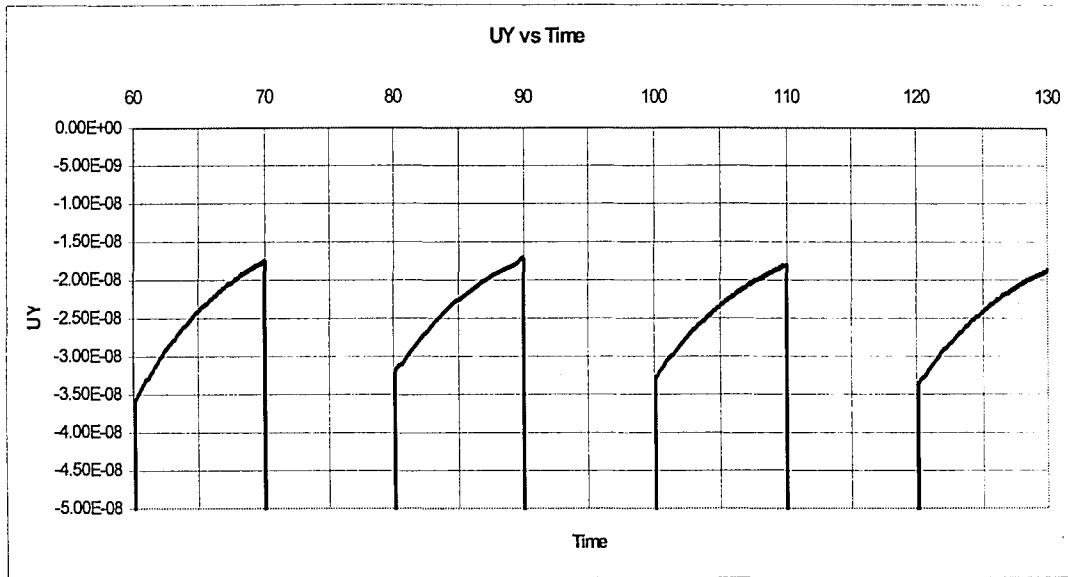
Figure 9.6: Relaxation curves for repeated hold and release 10 second cycles.

The results in this section demonstrate the cumulative viscoelastic material behavior that can occur under repeated cyclic loading. Note that, the displacements (not forces) are specified, and it is assumed that the membrane covers the entire surface of the lower electrode when it is pulled down. Thus, the numerical values obtained from this model should be considered representing of a conservative upper limit on the time dependent response.

10 Conclusion and Future Work

This study focused on the electromechanical behavior of RF MEMS Capacitive Switches. This included simulations to determine their natural frequencies, viscoelastic behavior and pull-in voltages. For all of the finite element simulations except the modal frequency simulation, the initial stress effect is not considered. The manufacturing process in responsible for the initial stress. Therefore, the results should be considered as a base line, or lower limit for the determined values.

All of the analyses in this research have been performed in order to aid a parallel experimental effort for better understanding of the switching behavior of RF MEMS Switches. There are four different membrane designs that were closely examined in this study.

Natural frequencies are calculated both with and without the initial stress effect. It is concluded that initial stress in the membrane increases the natural frequency drastically. The initial stress not only increases the natural frequency, but also the pull-in voltage. All the modal analyses were performed as in vacuum, therefore no damping effects are considered.

On the efforts to explore the viscoelastic behavior, the results demonstrated that although gold is not usually regarded as a viscoelasstic material, in its thin film form, it can behave in a manner similar to a classical viscoelastic material. By introducing the viscoelastic material properties to ANSYS, the results have shown that the switch recovers the elastic part immediately after release, but takes a finite time to fully come back to its original configuration.

The pull-in voltage determination and the switching simulation are both crucial for improving the needs of the RF MEMS industry. In the simulations performed, the pull-in voltage was obtained without including the initial stress effect. This is compared to the analytically determined (without initial stress) pull-in voltage. It was shown that the results are in good agreement. In addition, from the strength of materials calculations, pull-in voltage was calculated including the initial stresses. These values were also within the voltage range obtained in the experimental measurements at the Compound Semiconductor Technology Laboratory at Lehigh University.

For future analyses, the coupled simulation performed in this study can be applied to more complex geometries. Damping effects should be included for more realistic simulations. The most critical aspect of this study was the determination of the pull-in voltages for electrostatically actuated switches. Future studies can be performed to simulate the switch release behavior, in addition to more complex contact problems including dielectric charging phenomena.

References

1. Hsu, T.-R., *MEMS & Microsystems Design and Manufacture*. 2002: Mc Graw Hill.

2. Helvajian, H., *Microengineering Aerospace Systems*. 1999: AIAA.

3. Feynman, R.P., *"There's Plenty of Room at the Bottom"*. Presented at the American Physical Society Meeting in Pasadena CA, Dec 26,1959.

4. Howe, R.T., *Surface Micromachining for microsensors and microactuators* Journal of Vac. Sci. Technology, Dec 1988. **6**: p. 1809-1813.

5. *Wikipedia*. Available from: www.wikipedia.com.

6. *The Aerospace Coorparation*. Available from: www.aero.org.

7. Mansfield, B., *Fabrication of MEMS Devices*, New Jersey Nanotechnology Consortium.

8. E. Ngo, W.D.N., M.W. Cole, C. Hubbard and G. Hirsch K.P. Mohanchandra and G. P. Carman, *FABRICATION OF ACTIVE THIN FILMS FOR VIBRATION DAMPING IN MEMS DEVICES FOR THE NEXT GENERATION ARMY MUNITION SYSTEM*. DEC 2004, U. S. Army Research Laboratory, WMRD Weapons and Materials Research Directorate Aberdeen Proving Ground, MD 21005; Mechanical & Aerospace Engineering Department, University California at Los Angeles Los Angeles, CA 90095-1361.

9. Rebeiz, G.M., *RF MEMS Theory, Design, and Technology*. 2003: A John Wiley & Sons Publication.

10. Rebeiz, A.R.B.a.G.M., *A high -performance integrated K-Band diplexer*. IEEE Trans. Microwave Theory Tech., August 1999. **47**(8): p. 1477-1481.

11.   R. C. Ruby, A.B., C. Han, Y. Desai, F. Geefay, G. Gan, M. Gat and T. Verhoven. *High-Q FBarfilters in a wafer-level chip scale package.* in *IEEE International Solid State Circuits Conferance Digest.* 2002.

12.   F. D. Banon III, J.R.C., and C. T. C. Nguyen, *High-Q HF Microelectromechanical filters.* IEEE J. Solid State Circuits, April 2000. **35**(4): p. 512-526.

13.   Vietzorreck, L., *Modeling of the Millimeter-Wave Behavior of MEMS Capacitive Switches.* IEE MTT-S International, 1999. **4**: p. 1685-1688.

14.   C. Goldsmith, J.R., S. Eshelman ,T.H. Lin, D. Dennistor, S. Chen and B. Norvell, *Characterizations of Micromachined Switches at Microwave Frequencies.* IEE MTT-S International, 1996: p. 1141-1144.

15.   J. Y. Park, G.H.K., K. W. Chung, J. U. Bu,, *Electroplated RF MEMS Capacitive Switches.* IEE E Int. Conf. On Micro Electro Mechanical Systems, 2000: p. 639-644.

16.   Yao, J.J.a.C., *A Surface Micromachined Miniature Switches for Telecommunications Applications with Signal Frequencies from DC up to 4 GHz.* International Conf. Solid-State Sensors Actuators Digest, Stockholm, Sweden, 1995: p. 384-387.

17.   Becher, D., Chan, R., Hattendorf, M. and Feng, M.,, *Reliability Studies of Low-Voltage RF MEMS Switches.* GaAs Mantech Conference, San Diego, CA., 2002: p. 54-57.

18. Lei L. Mercado, S.-M.K., Tien-Yu Tom Lee, Lianjun Liu, *A Mechanical Approach to Overcome RF MEMS Switch Stiction Problem.* Electric Component and Technology Conference: p. 377383.

19. Palego, C., *RF MEMS technology for reconfigurable microwave applications*, in *FACULTE des SCIENCES et TECHNIQUES de LIMOGES.* 2006, UNIVERSITE DE LIMOGES.

20. Young, R.J.R.a.W.C., *Formulas for Stress and Strain, 6th Edition* ed. N.Y. McGraw -Hill. 1989.

21. Timoshenko, J.M.G.a.S.P., *Mechanics of Materials*, ed. B. PWS Publishing Company. 1997.

22. Kovacs, *Micromachined Transducers.* 1998: WBC/ McGraw-Hill, Boston.

23. *ANSYS®Academic Research, v. 11.0.*

24. *Science World.* Available from: http://scienceworld.wolfram.com.

25. Cristiano Palego, S.H., Bora Baloglu, Zhen Peng, James C. M. Hwang, Herman F. Nied, David I. Forehand, Charles L. Goldsmith, *Microwave Intermodulation Technique for Monitoring the Mechanical Stress in RF MEMS Capacitive Switches.* submitted to IEEE, International Microwave Symposium, Atlanta 2008

Vita

Bora Baloglu was born on July 05, 1980 in Eskisehir, Turkey to Nevin and Mustafa Baloglu. He has lived in Eskisehir most of his life, and attended to Kilicoglu Anatolian High School between 1991 and 1998. He completed his Bachelor of Science in Mechanical Engineering at Eskisehir Osmangazi University in June 2004.

Bora came to the United States in January 2005 and prior to starting his studies at Lehigh University, enrolled in ESL classes at Lehigh University. Right after he completed his English Proficiency classes in September 2005, he began his graduate studies towards a Master of Science degree in Mechanical Engineering, and expects to graduate in January 2008.

END OF
TITLE